



Analysis of the As-Cast Microstructure and Properties of the Ni-Based Superalloy MAR-M247[®] Produced *Via* Directional Solidification

ŁUKASZ RAKOCZY, MAŁGORZATA GRUDZIEN-RAKOCZY, RAFAŁ CYGAN, TOMASZ KARGUL, ŁUKASZ MAJ, and ANNA ZIELIŃSKA-LIPIEC

The presented research investigates MAR-M247[®] Ni-based superalloy castings produced *via* directional solidification at various mold preheating temperatures (1510, 1566 °C) and withdrawal rates (3.4, 5.0 mm/min). Casting analyses were carried out *via* thermodynamic simulations, differential scanning calorimetry (DSC), X-ray diffraction (XRD), light microscopy (LM), scanning electron microscopy (SEM), energy dispersive X-ray spectroscopy (EDX), scanning transmission electron microscopy (STEM), and tensile testing. On DSC curve, four effects have been registered during cooling: liquidus (1337 °C), formation of eutectic $\gamma - \gamma'$ (1315 °C), precipitation of $\text{Ni}_7(\text{Hf}, \text{Zr})_2$ (1244 °C), and M_5B_3 borides (1201 °C). The castings' primary and secondary dendrite arm spacing decreases with increasing withdrawal rates for both shell mold temperatures. The dendritic regions of the castings are characterized by a relatively homogenous microstructure, consisting of γ' precipitates surrounded by the matrix, with a mean size in the range of 0.437 to 0.481 μm , depending on the casting parameters. In the interdendritic spaces, $\gamma - \gamma'$ eutectic, MC carbides, M_5B_3 , $\text{Ni}_7(\text{Hf}, \text{Zr})_2$, and M_3C_2 phases were identified. The ultimate tensile strength of the produced castings was in the range of 970 to 1088 MPa.

<https://doi.org/10.1007/s11661-023-07123-8>
© The Author(s) 2023

I. INTRODUCTION

DIRECTIONALLY solidified (DS) Ni-based superalloys are widely used in aircraft turbine engines, especially for the fabrication of large-scale and complicated blades, due to their higher casting efficiency and simpler orientation requirements than single-crystal superalloys.^[1,2] In the columnar grain microstructure of superalloys, grain boundaries transverse to the Z-axes, where the principal stress is active, are eliminated. This allows for a decrease in cavitation and

cracks at the boundaries, increasing high-temperature strength. The parallel aligning of grain boundaries to the casting's z-axis is most favorably achieved *via* solidification, *i.e.*, high-energy, liquid \rightarrow solid phase transformations in superalloys.^[3,4] By inducing solidification under controlled thermal gradient conditions, it is possible to produce elongated grains aligned parallel to the gradient. Gaining detailed information about the solidification path is crucial in the characterization of the primary microstructure, especially directionally solidified superalloys, as well as determining the influence of phase transformations occurring during heat treatment on the aerospace component's final strength.

Several manufacturing parameters have an effect on the cooling rate, which influences the dendritic microstructure of superalloys, microsegregation of alloying elements, and consequently the material's mechanical properties.^[5-7] Nawrocki,^[8] based on experiments on IN713C castings, stated that the wall thickness of the casting has the greatest impact on the average cooling rate of the equiaxed grains. The dendritic growth in Ni-based superalloys promotes microsegregation that greatly affects the formation and distribution of the second precipitate phases in the as-cast state. In the marginal case, element microsegregation can lead to structure defects, such as hot tears, misruns, and freckle

ŁUKASZ RAKOCZY, TOMASZ KARGUL, and ANNA ZIELIŃSKA-LIPIEC are with the Faculty of Metals Engineering and Industrial Computer Science, AGH University of Science and Technology, Mickiewicza 30, 30-059 Kraków, Poland. Contact e-mail: lrakoczy@agh.edu.pl MAŁGORZATA GRUDZIEN-RAKOCZY is with the Łukasiewicz Research Network-Kraków Institute of Technology, Zakopiańska 73, 30-418 Kraków, Poland. RAFAŁ CYGAN is with the Investment Casting Division, Consolidated Precision Products Corporation, Hetmańska 120, 35-078 Rzeszów, Poland. ŁUKASZ MAJ is with the Institute of Metallurgy and Materials Science, Polish Academy of Sciences, Reymonta 25, 30-059 Kraków, Poland.

Manuscript submitted March 15, 2023; accepted June 24, 2023.

Article published online July 20, 2023

defects, making it impossible to achieve an acceptable casting quality level.^[9] Obtaining a better understanding of the microstructure's response to casting conditions and parameters would enable optimizing the technological and mechanical properties of the superalloy.^[10] Li^[11] observed that an increase in withdrawal rate during the casting of the IN713C Ni-based superalloy can raise its tensile strength at 800 °C. Changing the withdrawal rate from 10 to 50 $\mu\text{m/s}$ allowed to refine the microstructure, resulting in a higher yield (11.8 pct) and ultimate strength (18.3 pct). When the withdrawal rate was set to 100 $\mu\text{m/s}$, the superalloy's microstructure was characterized by an excessive volume fraction of eutectic $\gamma - \gamma'$ islands and Mo/Cr borides. Liu,^[12] based on results of X-ray microtomography and the U-net convolutional neural network, observed that the increase in cooling rate of the single-crystal superalloy (DD5) leads to a decrease in MC carbide size and volume fraction. Zhao^[13] reported that increased withdrawal rates of single-crystal superalloys refine the microstructure, decrease the distance between primary dendrites, favor the growth of arm dendrites (secondary and tertiary), reduce alloying element segregation, and allow to obtain finer γ' precipitates. The lowest reported casting porosity after solidification was attained for a withdrawal rate of 4.5 mm/min. These findings show that by changing the casting parameters, it is possible to steer the microstructure and mechanical properties over a wide range, which is highly advantageous for the production of aerospace components.

In industrial practice, the MAR-M247[®] Ni-based superalloy is used in fully heat-treated condition. Solution treatment partially homogenizes the microstructure and subsequent aging allows to obtain a high volume fraction of cube-shaped γ' precipitates. Therefore, obtaining more information on the superalloy's microstructure and properties in the as-cast state (reference) is essential to properly design and control subsequent heat treatment. Solidification segregation of the elements between dendritic and interdendritic spaces induces the formation of non-equilibrium phases, such as carbides, eutectic phases, or other low melting point phases, which should be dissolved during homogenization. With that in mind, the main aim of this work was to characterize solidification behavior of DS MAR-M247[®] Ni-based superalloy and clarify the effect technological parameters on the as-cast microstructure and resulting mechanical properties.

II. MATERIALS AND METHODOLOGY

The selected cast and gating system material was the DS MAR-M247[®] (registered trademark of the Martin Marietta Corporation) Ni-based superalloy. The nominal material's chemical composition is presented in Table I. The whole investment casting process was performed in the R&D Laboratory for Aerospace Materials at Rzeszów University of Technology (Poland). The setup consisted of a cooling base plate, construction pin, pouring pan, and research castings. In addition, wax sets were reinforced with ceramic rods to

stiffen their structure, and a specially designed holder allowed mounting the sets in a robotic stand for washing and multi-layered ceramic mold manufacturing. The geometries of the 8 wax pattern rods were $\varnothing 14 \text{ mm} \times 250 \text{ mm}$, with vents developed to stabilize and strengthen the wax model and facilitate correct dewaxing. The molds were produced through a “dip and stucco” method. Each layer was formed by dipping the wax pattern into a slurry (binder and filler) and then covering it by a coarse dry backup. After drying, the molds were dewaxed in a boiler clave and burnt out to remove any residual wax. Finally, they were covered by alumina silicate Fiberfrax[®] (registered trademark of the UNIFRAX I LLC) heat insulation. The directional solidification of the MAR-M247[®] Ni-based superalloy was carried out in a vertical Bridgman vacuum furnace ALD VIM-IC 2 E/DS/SC.

Each ceramic mold was placed in the furnace chamber and preheated to either $T_0 = 1510 \text{ °C}$ or 1566 °C (Table II). The 4.5 kg ingot was inductively melted in a vacuum of $2.9 \times 10^{-3} \text{ Pa}$. After heating the furnace to 1600 °C and holding for 30 minutes, the withdrawal was initiated at a predetermined rate ($v_s = 3.4$ or 5.0 mm/min). After solidification and cooling to room temperature, each mold was knocked out and the cast rods were cut off. The castings were designated as LP3W, LP5W, HP3W, and HP5W. “LP” or “HP” refers to the lower or higher shell mold preheating temperature, while “3W” or “5W” indicates the withdrawal rate of 3.4 or 5.0 mm/min.

The Thermo-Calc[®] (registered trademark of the Thermo-Calc Software AB, Sweden) software (version 2021a), with the TCNI10 database, was used to analyze the solidification process of the DS MAR-M247[®] using the Scheil model. The Scheil model considers the segregation of solute elements during solidification and assumes the absence of back-diffusion during calculations.^[14] Complete solidification is assumed when less than 1 pct liquid is present in the calculation, and generally, the solidification range is quite broad.^[15,16] In this paper, the model was used to predict the type of primary phases in the as-cast superalloy.

Differential scanning calorimetry (DSC) was used to determine phase transformation temperatures and the accompanying thermal effects during sample solidification. Experiments were carried out using a Netzsch STA 449F3 Jupiter device, equipped with a rhodium furnace operating up to 1600 °C , and a microbalance with a mass resolution of 10^{-6} g and a calorimetric sensitivity of 0.1 mW. Before measuring, the device was calibrated by recording the temperatures and melting enthalpies of pure standard materials (In, Sn, Al, Au, Ni). All values recorded from the DS MAR-M247[®] superalloy were corrected for the values resulting from the device calibration, which enabled the quantitative analysis of the thermal melting/solidification effects. Next, the furnace chamber was twice evacuated, and the measurement space was filled with inert gas. A zirconium oxygen trap was additionally placed in the chamber to bind residual oxygen and reduce sample oxidation. The samples were placed in Al_2O_3 85 μL crucibles with lids and transferred to the chamber. The program included

Table I. Nominal Chemical Composition of the DS MAR-M247[®] Ni-Based Superalloy, Wt Pct

Element	Co	W	Cr	Al	Ta	Hf	Ti	Mo	Zr	B	C	Ni
Concentration	10.0	10.0	8.40	5.50	3.0	1.4	1.1	0.65	0.05	0.015	0.15	bal.

Table II. Selected Casting Parameters

Casting	Shell Mold Preheating Temperature, °C	Pouring Temperature, °C	Withdrawal Rate, mm/min
LP3W	1510		3.4
LP5W			5.0
HP3W	1566	1538	3.4
HP5W			5.0

heating the sample in an inert atmosphere (argon, 6 N purity) from room temperature to 1460 °C with a heating rate 10 K/min, holding for 3 min, and then cooling to room temperature with cooling rate 10 K/min. In the high-temperature range, phase transformation temperatures may be disturbed by ongoing sample oxidation processes, above the liquidus temperature of the alloy. Therefore, sample mass changes were tracked in addition to registering thermally activated effects. No mass variations were observed, proving negligible oxidation and chemical composition changes of superalloy during DSC.

X-ray diffraction (XRD) was carried out to identify the castings' phases. Specimens with dimensions of $\varnothing 14 \times 10$ mm and mechanically polished surfaces were prepared. Measurements were performed at room temperature in Bragg-Brentano geometry using a Bruker D8 Advance diffractometer, equipped with cobalt radiation ($\lambda = 1.789$ Å), in the range of $2\theta = 20^\circ$ to 130° in steps of 0.04° .

Metallographic specimens were cut off from each of the four castings (to dimensions $\varnothing 14 \times 5$ mm), ground with SiC sandpaper and polished using diamond suspensions (3 μm , 1 μm) and colloidal silica (0.06 μm). Light microscopy (LM) observations were performed using a Leica DM1000 microscope on specimens chemically etched in reagent No. 17 (25 mL water, 25 mL HCL, 25 mL HNO₃, 1.5 g H₂MoO₄) for 5 seconds.

The Thermo Scientific Phenom XL G2 scanning electron microscope (SEM), with 20 kV accelerating voltage and a backscattered electrons (BSE) detector, was used for further observations. Quantitative analysis of the γ' precipitates and MC carbides was performed using the ImageJ commercial software (National Institutes and the Laboratory for Optical and Computational Instrumentation, University of Wisconsin, Madison, WI). The volume fraction of γ' precipitates and MC carbides was estimated using the planimetric method Eqs. [1] and [2]:

$$V_v = A_A, \quad [1]$$

$$A_A = \left(\frac{\sum A_i}{A} \right) * 100\text{pct}, \quad [2]$$

where V_v —total volume of the phase object per unit volume of the superalloy, $\mu\text{m}^3/\mu\text{m}^3$, A_A —total field flat sections on the individual phase of the image per unit area, $\mu\text{m}^2/\mu\text{m}^2$, A_i —total field of flat sections on the individual i-phase, μm^2 , A —total image area, μm^2 . It was assumed, based on the Cavalieri-Hacquet principle that the relative volume taken up by a given microstructure's constituent is the area's fraction occupied by this constituent on the unit plane of the specimen. The following magnifications were used: 1000 times—total area 72297 μm^2 (MC carbides) and 25,000 times—total area 114.49 μm^2 (γ' precipitates). The size of secondary γ' precipitates in dendritic regions and interdendritic spaces was represented as the side of the cuboidal precipitates (square root of precipitates' area) Eq. [3]. The measurements were carried out in 25 locations (more than 10,000 precipitates), based on images captured at 25,000 times magnification (area 114.49 μm^2). SEM-BSE images were binarized and subjected to a de-speckle filter, which removed noise without edge blurring.

$$\bar{D} = \bar{d} = \sqrt{A}. \quad [3]$$

X-ray dispersive spectroscopy (SEM-EDX) was performed to determine the distribution of selected alloying elements. Distribution maps and quantitative analyses of selected areas were performed (ZAF correction). The calculation of the partitioning coefficient of the alloying elements was carried out in accordance with the relationship:

$$k^i = \frac{C_D^i}{C_0^i}, \quad [4]$$

where C_D^i —i-element concentration in the dendrite core (point analysis), C_0^i —i-element concentration in the area with dimensions 53×53 μm (area including dendritic

cores and interdendritic spaces). The partitioning coefficient of each alloying element was calculated based on 40 measurements at various locations. The measurement duration for the point and area scans was 90 seconds ($>$ one million counts), and for maps, it was approx. 1 hour. TEM/STEM (transmission/scanning transmission electron microscopy) was carried out using the FEI Tecnai G2 SuperTWIN 200 kV FEG microscope, equipped with a SIS MegaView III camera for bright-field (BF) microstructure and selected area electron diffraction (SAED) pattern acquisition, as well as a Fishione detector for high-angle annular dark-field (HAADF) STEM observations. The JEMS software (JEMS-SWISS, Jongny, Switzerland) was applied for phase analysis from the gathered SAED patterns. TEM/STEM lamellae were cut out and polished with a Ga^+ ion beam in a ThermoFisher Scios 2 Dual Beam microscope. The lamellas were ion polished down to a thickness of 100 nm. Directly before mounting in the microscope column, the samples were subjected to plasma cleaning to remove surface contaminations. Room-temperature tensile testing was carried out on round-threaded specimens using a Zwick 250 kN device. The test samples were prepared in accordance with the requirements of ASTM E8/E8M (diameter 6 mm, gage length 30 mm). Before testing, the samples were loaded with an initial force of 2200 N, and the tests were performed at a constant rate of 0.004.

III. RESULTS AND DISCUSSION

A. Analysis of the Solidification Characteristics Obtained Via Thermo-Calc[®] Simulations and DSC

Based on the DS MAR-M247[®] Ni-based superalloy's chemical composition, a thermodynamic simulation of the solidification process (based on the Scheil method) was performed (Figure 1). According to the simulation, superalloy crystallization (γ phase formation) begins at 1397 °C. With the decrease in temperature, the solubility of alloying elements (such as Hf, Ta, W, C, and B) in the matrix is reduced, inducing their segregation at the γ

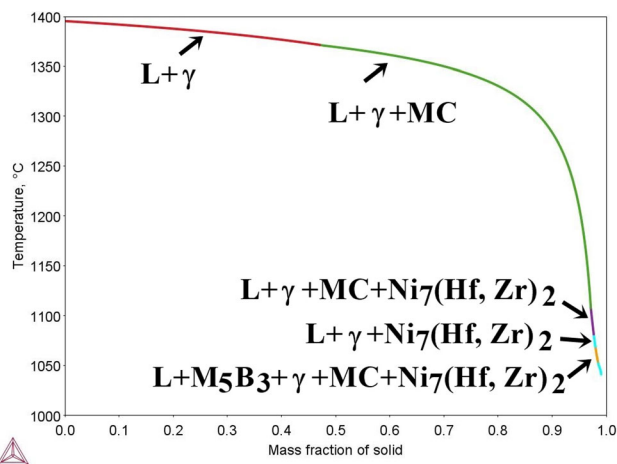


Fig. 1—Solidification simulation results obtained via Thermo-Calc[®].

phase dendrite–interdendritic liquid interface. After reaching a γ phase mass fraction of 0.47 at 1371 °C, the precipitation of MC carbides from the liquid occurs, which is most favorable in interdendritic spaces (according to the typical reactions $\text{L} \rightarrow \text{MC}$ or $\text{L} \rightarrow \gamma + \text{MC}$). These areas offer some solubility of other carbide-forming elements, such as Hf, Ta, Ti, W, or Cr. The formation of MC in the interdendritic liquid depletes these elements and enriches them with Al, which is a strong γ' former. During subsequent cooling, the precipitation of $\text{Ni}_7(\text{Hf}, \text{Zr})_2$ from the liquid takes place. It should be noted that the Ni_7Hf_2 and Ni_7Zr_2 phases have the same crystallographic structure (monoclinic system, C12/m1 space group) and can dissolve each other. As the temperature drops, the process of MC carbide formation ends. The last precipitated phase is M_5B_3 . Secondary γ' precipitates are not included in the results as they only start to precipitate in solid state from a supersaturated matrix.

Figure 2 shows the DSC curve of the MAR-M247 superalloy during cooling, where the main phase transformation temperatures were determined. The 1st effect at 1337 °C is related to the start of the solidification process. The 2nd exothermic effect at 1315 °C probably originates from the eutectic phase transformation $\text{L} \rightarrow \gamma + \gamma'$. It cannot be excluded that MC carbide formation overlaps with this effect. Usually, a certain amount of carbides can precipitate directly from the liquid at the beginning of the solidification process, while those with much more complex morphologies generally form through the phase transformation $\text{L} \rightarrow \gamma + \text{MC}$ at the final process stage. This effect can be covered with the formation temperature of the $\gamma - \gamma'$ eutectic phase. Below 1250 °C, further two disturbances were revealed on the DSC cooling curve [Figure 2(b)]. These are of lower intensity compared to the solidification peak and are caused by the formation of subsequent minor phases. The 3rd effect registered at 1244 °C (-1.299 J/g) most likely corresponds to the formation of the $\text{Ni}_7(\text{Hf}, \text{Zr})_2$ intermetallic phase, whereas the 4th effect at 1201 °C (-7.374 J/g) is linked with the precipitation M_5B_3 borides from the residual liquid.

B. Castings Microstructure Characterization

Based on the obtained X-ray diffractograms (Figure 3), the following phases were identified in all castings: γ matrix, intermetallic γ' phase, MC carbides, M_5B_3 borides, and the $\text{Ni}_7(\text{Hf}, \text{Zr})_2$ intermetallic phase.

The chemically etched specimens were analyzed via LM and revealed a typical dendritic structure (Figure 4). The dendritic areas (primary dendrites and secondary dendrite arms) are characterized by a relatively homogeneous microstructure, while numerous eutectic $\gamma - \gamma'$ islands and carbide-looking precipitates are located in interdendritic spaces. Based on the captured images, the primary dendrite arm (PDAS) and secondary dendrite arm spacings (SDAS) were measured, and it can be seen that the withdrawal rate and mold preheating temperature influenced these values. The PDAS and SDAS values tend to be lower with increasing withdrawal rate for both mold preheating temperatures. In the case of

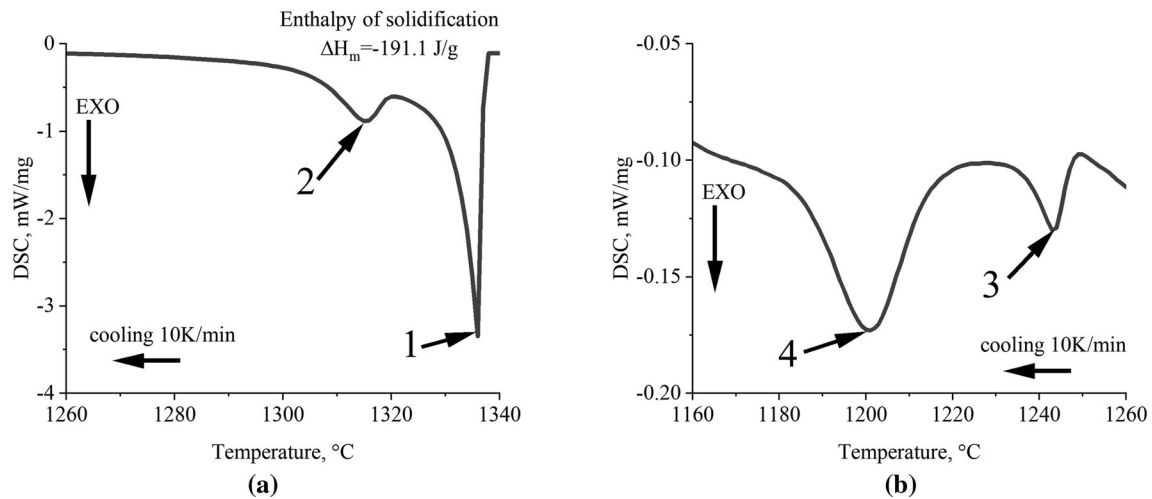


Fig. 2—DSC curve of the DS MAR-M247[®] Ni-based superalloy registered during cooling: (a) 1340–1260 °C; (b) 1260–1160 °C.

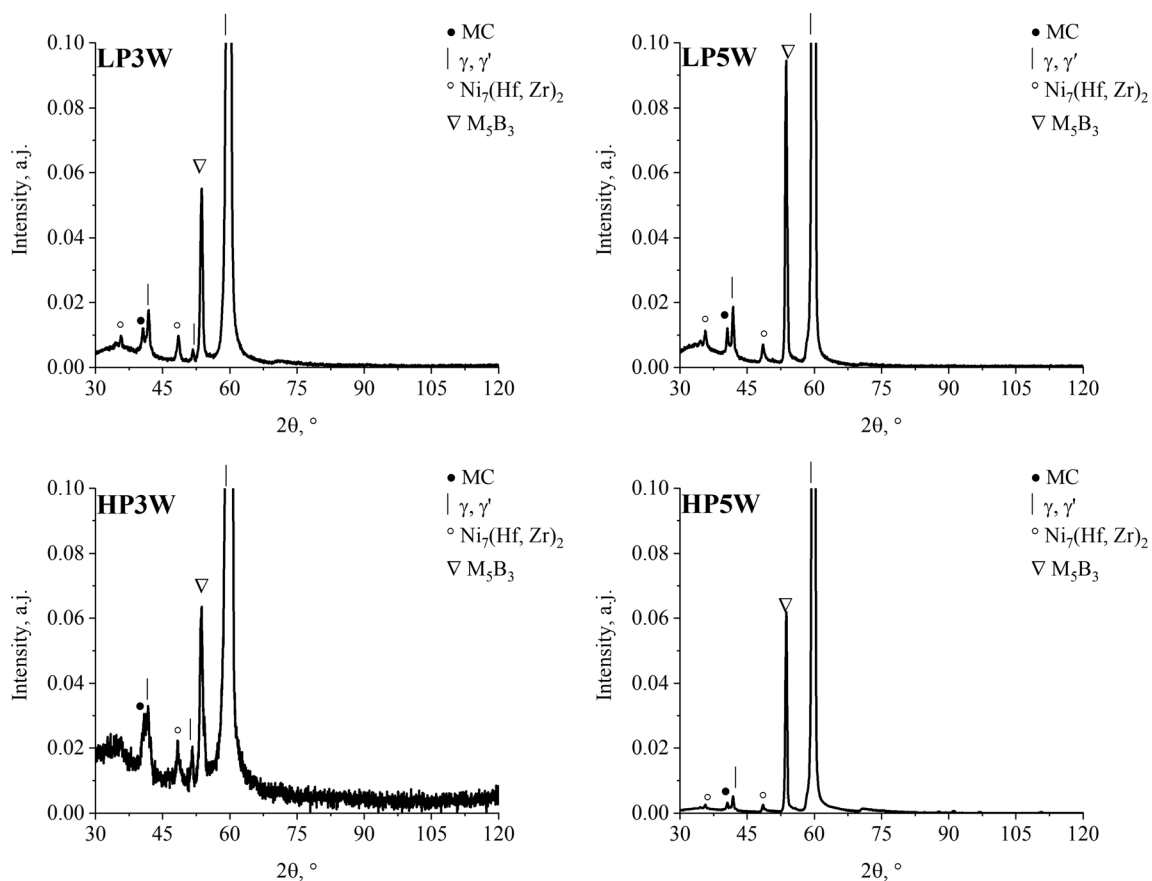


Fig. 3—XRD patterns of the DS MAR-M247[®] castings.

the preheat temperature of 1510 °C (< pouring temperature), a withdrawal rate of 3.4 mm/min was selected, which enabled obtaining PDAS and SDAS values of 325 μm (± 31 μm) and 64 μm (± 8 μm), respectively. For the withdrawal rate of 5.0 mm/min, the registered values were PDAS 303 μm (± 34 μm) and SDAS 56 μm (± 6 μm). For the preheat temperature of 1566 °C (> pouring temperature) the PDAS and SDAS were

331 μm (± 33 μm) and 71 μm (± 6 μm), respectively, for a withdrawal rate of 3.4 mm/min, while for the 5.0 mm/min, the values were 315 μm (± 31 μm) and 60 μm (± 7 μm). In other words, for a constant withdrawal rate, a higher mold preheating temperature leads to increased PDAS and SDAS values. The intergranular region's area decreases with the increase

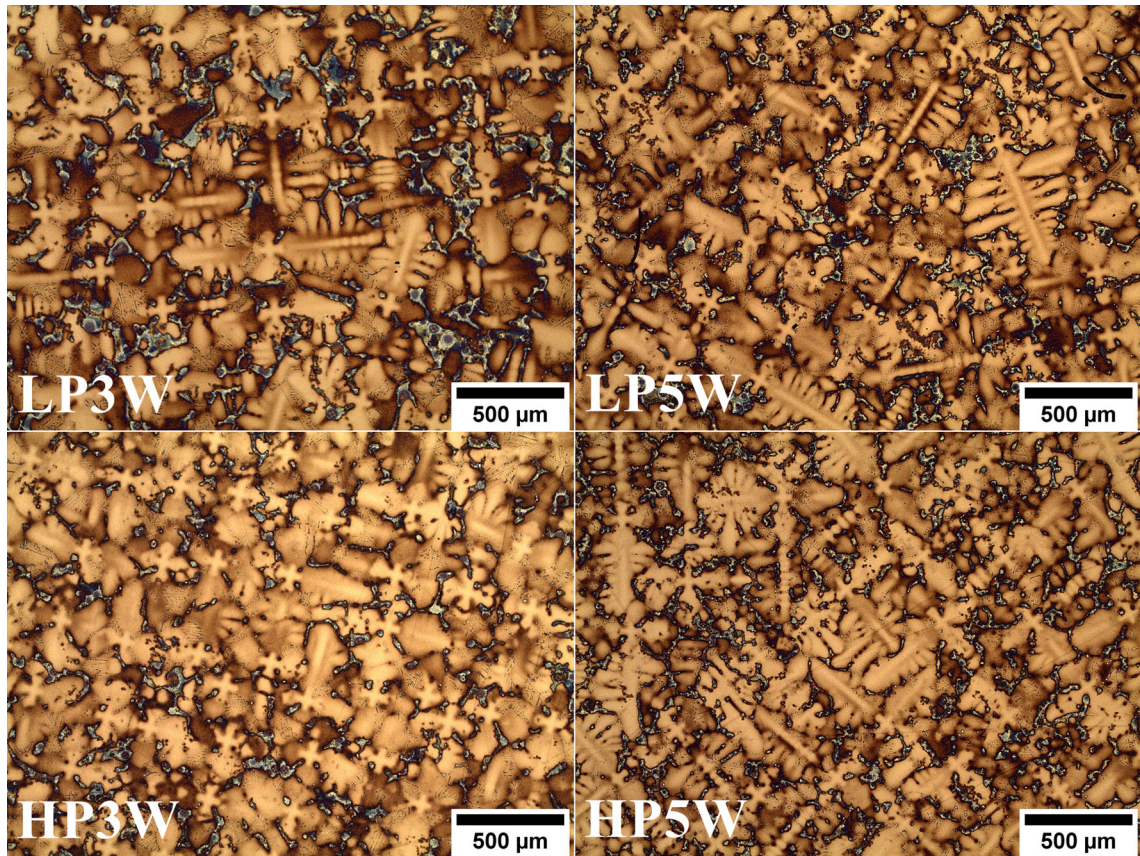


Fig. 4—Dendritic microstructure of the as-cast DS MAR-M247® castings.

in the withdrawal rate, mainly due to the withdrawal rate changing the primary dendritic arm spacing.

C. Partitioning Coefficients Analysis

To reveal the distribution of alloying elements in the castings' microstructure, a semi-quantitative analysis of the chemical composition was performed using SEM-EDX. Based on the obtained data, the partitioning coefficient $k^i = \frac{C_i^d}{C_i^0}$ was calculated Eq. [4]. The partitioning coefficients k^i for the selected elements are shown in Table III. The values of $k^i > 1$, indicating a higher concentration of the element in the dendritic region, are mainly observed for W and Al. As the mobility of W is very sluggish, its diffusion from the liquid into the matrix is not fully obtained using usual cooling rates. A similar $k^W > 1$ was detected in the heat-treated René 108 Ni-based superalloy, in which W enrichment of the dendritic region led to the formation of M_5B_3 nanoborides at the interfaces of the γ matrix and secondary γ' precipitates.^[17] This suggests that such strong segregation would be difficult to reduce even after heat treatment. Coefficients $k^i < 1$ are obtained for Cr, Ti, Ta, and Hf. These carbide formers tend to strongly segregate in the residual liquid that forms during casting solidification. Hence, the interdendritic regions become the preferred place for carbide nucleation and subsequent growth. With increasing withdrawal rates, the

number of secondary dendritic arms also increases.^[18] This can effectively suppress elemental diffusion and trap numerous carbide-forming elements in interdendritic regions. This is especially true for Ta and Hf, which are strong carbide formers; therefore, the presence of carbides in interdendritic spaces is expected. The values of the k^{Ni} and k^{Co} coefficients, *i.e.*, the elements included in the γ phase, are close to 1, indicating their relatively homogenous distribution in the castings, which is typical for the matrix phase.

D. γ' Precipitates Morphology Characterization

The morphologies of the primary γ' precipitates are shown in Figure 5. They were formed through the $L \rightarrow \gamma + \gamma'$ phase transformation. The amount of these precipitates is significant, which indicates a strong enrichment of the residual liquid phase in γ' -formers. The precipitates are characterized by a diversified distribution and complex morphologies. According to Sims,^[3] the presence of Hf in DS superalloys favors the formation of higher amounts of γ' primary precipitates. Although the eutectic $\gamma - \gamma'$ is an undesirable component in Ni-based superalloys, its complete dissolution in the matrix during supersaturation may prove impossible due to the risk of incipient melting. With the strong variation in precipitate size, the analysis of stereological parameters was not carried out. To compare the γ' precipitates of the produced castings, 20

Table III. Partitioning Coefficients of Selected Alloying Elements Calculated Based on the SEM-EDX Measurements

Variant	k^{Ni}	k^{Co}	k^{Cr}	k^{W}	k^{Mo}	k^{Ti}	k^{Hf}	k^{Ta}	k^{Al}
LP3W	0.99 (± 0.02)	1.02 (± 0.04)	0.98 (± 0.07)	1.18 (± 0.13)	1.13 (± 0.25)	0.89 (± 0.24)	0.59 (± 0.31)	0.99 (± 0.12)	1.06 (± 0.06)
LP5W	1.00 (± 0.02)	0.99 (± 0.05)	0.94 (± 0.07)	1.13 (± 0.22)	1.18 (± 0.43)	0.91 (± 0.25)	0.63 (± 0.29)	0.99 (± 0.08)	1.06 (± 0.07)
HP3W	1.00 (± 0.02)	0.98 (± 0.05)	0.92 (± 0.10)	1.11 (± 0.25)	1.07 (± 0.31)	0.96 (± 0.13)	0.79 (± 0.29)	0.99 (± 0.09)	1.09 (± 0.08)
HP5W	0.99 (± 0.03)	1.01 (± 0.06)	0.97 (± 0.11)	1.26 (± 0.15)	1.01 (± 0.19)	0.84 (± 0.17)	0.60 (± 0.27)	0.96 (± 0.06)	1.04 (± 0.13)

semi-quantitative chemical composition analyses were performed for each variant. Based on the obtained data (Table IV), it can be observed that the γ' precipitates are mainly composed of Ni and Al. The concentration relationship between these elements in the castings is very similar. The γ' -formers in the Ni-based superalloys are Al, Ti, Ta, and Hf. Therefore, the relationship (Ni, Co)/(Al, Ti, Ta, Hf) was also calculated, which is almost the same for all tested castings.

The secondary γ' precipitates are the dominant component in the microstructure, and their stereological parameters were investigated (separately for dendritic regions and interdendritic spaces) (Figure 6). The mean volume fraction and standard deviation of the secondary γ' precipitates in the dendritic region decreased with increasing withdrawal rate for both mold preheating temperatures, while higher preheating allowed obtaining higher volume fractions [Figure 7(a)]. For 1510 °C, the increase in withdrawal rate from 3.4 to 5.0 mm/min led to a decreased volume fraction from 51 to 50 pct, while for 1566 °C the observed change was from 53 to 51 pct. The volume fraction of secondary γ' precipitates in the interdendritic spaces in each variant is higher compared to the dendritic regions [Figure 7(b)]. The highest volume fraction of secondary γ' precipitate, *i.e.*, 57 pct (4 pct more compared to the dendritic region) was obtained in casting HP3W ($T_0 = 1566$ °C, $v_s = 3.4$ mm/min). Increasing the withdrawal rate to 5.0 mm/min caused a slight decrease in volume fraction to 56 pct. A similar trend was observed for castings LP3W and LP5W ($T_0 = 1510$ °C), where the volume fraction also dropped by 1 pct for the longer withdrawal rate from 53 to 52 pct. The precipitates' morphology is more complex and are characterized by a slightly more significant variation in size. Provided that a unidirectional heat flow is imposed, the product of the temperature gradient and withdrawal is equivalent to the cooling rate. The morphology of the secondary γ' precipitates resembles a cube. The deviation from the cubic shape occurs with increasing precipitate size. It should be noted that the morphology of γ' depends on the local thermodynamical conditions determined by the chemical composition, state of elastic stresses, and the mutual interaction between the precipitates. These factors change as a function of temperature and are conditioned by the system's attempt to achieve thermodynamic equilibrium.

The mean size of the secondary γ' precipitates, expressed as the equivalent side of the square, was calculated to quantitatively analyze the influence of mold preheating temperature and withdrawal rate. Figure 8 shows the distribution of the mean size of the secondary γ' precipitates and fitted curves representing their log-normal distribution. The highest mean value of the precipitate size, *i.e.*, 0.481 μm , was obtained in casting HP3W ($T_0 = 1566$ °C), which is also characterized by the highest PDAS and SDAS values. The increase in withdrawal rate to 5.0 mm/min led to a decrease in the mean γ' precipitate size to 0.457 μm . For the lower T_0 temperature, the increase in withdrawal rate from 3.4 to 5.0 mm/min caused the mean γ' precipitate size to decrease from 0.465 μm to 0.437 μm .

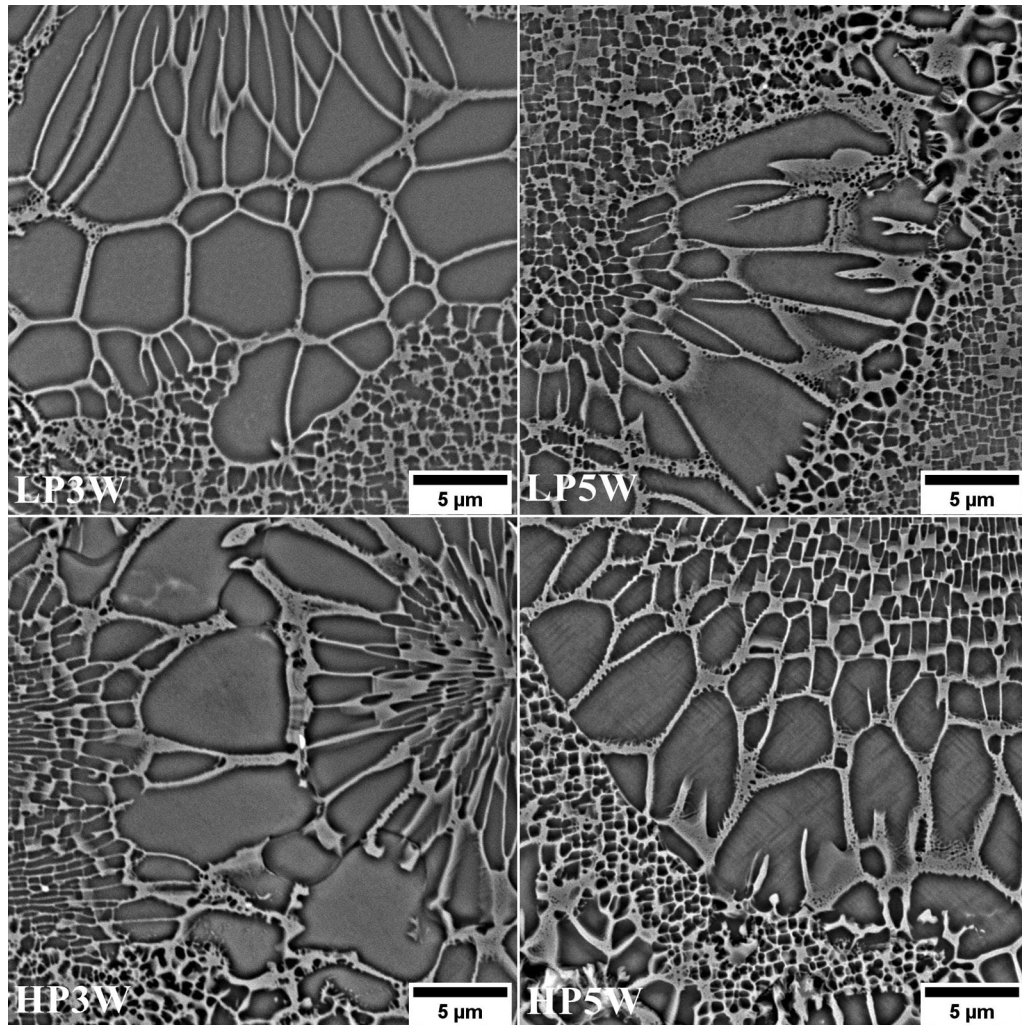


Fig. 5—Morphology of the primary γ' precipitates in as-cast DS MAR-M247[®] castings, SEM-BSE.

The secondary γ' precipitates in the interdendritic spaces were subjected to a similar image analysis. Figure 9 summarizes the mean size of all analyzed secondary γ' precipitates in the interdendritic regions, including fitted curves representing their log-normal distribution. In castings LP3W and LP5W ($T_0 = 1510$ °C), the increase in withdrawal rate led to a decrease in the mean size of secondary γ' precipitates from 0.604 to 0.565 μm . Casting HP3W was characterized by the largest mean size of 0.634 μm , while for casting HP5W, it was 0.595 μm .

In general, it is possible to determine the microstructural evolution of complex alloys, such as Ni-based superalloys, by tracking their internal energy,^[19–21] as shown in Eq. [5]. It is widely accepted that minimizing the sum of elastic strain energy and surface energy determines the shape of single γ' precipitates.

$$E_{\text{total}} = E_{\text{str}} + E_{\text{surf}} + E_{\text{int}}, \quad [5]$$

where E_{str} —elastic strain energy caused by the lattice misfit between γ' precipitate and γ matrix, E_{surf} —surface energy (interfacial energy) of the γ' precipitate, E_{int} —elastic interaction energy between γ' precipitates.

E_{total} —energy state, E_{str} —elastic strain energy caused by lattice misfit between γ' precipitates, and the γ matrix, E_{surf} —surface energy (interfacial energy) of the γ' precipitates, E_{int} —elastic interaction energy between γ' precipitates. Grosdidier^[19] indicated that the morphology transformations sphere \rightarrow cube \rightarrow octocube proceed quickly as the process is controlled by an interfacial reaction. Here, the frequency of atomic jumps through the interface is essential, rather than long-distance diffusion. Sims^[3] reported that slower cooling rates during the DS process result in a coarser solid-state cuboidal γ' directly in an as-cast state, which is in line with our observations.

E. Characterization of the MC Carbides and Minor Phases

Casting solidification is associated with alloying element segregation, verified by the calculated partitioning coefficient values. This favors the formation of minor phase precipitates in close proximity to eutectic $\gamma - \gamma'$ islands. The observed MC carbides (Figure 10, bright phase contrast) are characterized by complex

Table IV. Results of Primary γ' Precipitates Semi-quantitative SEM-EDX Analysis, At Pct

Casting/Element	Ni	Al	Co	Cr	Ta	Ti	Mo	Hf	Ni/Al	(Ni, Co)/ (Al, Ti, Ta, Hf)
LP3W	63.9 (± 1.2)	17.6 (± 0.7)	7.1 (± 0.5)	4.3 (± 1.0)	2.7 (± 0.2)	2.1 (± 0.3)	0.5 (± 0.2)	1.7 (± 0.3)	3.6 (± 0.2)	2.9 (± 0.1)
LP5W	64.0 (± 0.9)	17.7 (± 0.6)	7.0 (± 0.2)	4.2 (± 0.6)	2.7 (± 0.2)	2.0 (± 0.2)	0.4 (± 0.1)	1.9 (± 0.6)	3.6 (± 0.2)	2.9 (± 0.1)
HP3W	64.4 (± 0.6)	17.3 (± 0.7)	7.0 (± 0.2)	4.1 (± 0.4)	2.7 (± 0.2)	2.1 (± 0.2)	0.5 (± 0.2)	2.0 (± 0.5)	3.7 (± 0.2)	3.0 (± 0.1)
HP5W	64.6 (± 0.8)	17.0 (± 0.7)	7.1 (± 0.2)	4.3 (± 0.3)	2.7 (± 0.2)	2.1 (± 0.2)	0.5 (± 0.2)	1.8 (± 0.2)	3.8 (± 0.2)	3.0 (± 0.1)

morphologies, including blocky-shaped, sharp-edged parallelograms and Chinese script-like (feather-, herringbone-like). Other important factors influencing MC carbide morphologies are solidification parameters, such as growth rates and thermal gradients. According to Bhambri,^[22] the carbide's morphology changes from octahedron to arrowed shape and finally to Chinese script-like with increasing cooling rates. Carbides growing at slow cooling rates are close to equilibrium, and their shape is an octahedron. If the cooling rate increases and the carbide growth rate increases, ensuring sufficient carbide-forming element diffusion, the formation of equilibrium shaped carbides becomes more challenging. The carbide's growth is then influenced by the direction of heat flow and carbide-forming element distribution, resulting in irregular carbides. D'Souza^[23] proved that the tip of the secondary dendrite has a greater cooling rate than its root. Therefore, carbides shaped at the root of the second dendrite are octahedral blocks, whereas carbides at the dendrite's tip, where the cooling rate is faster, are mostly strips. Dendritic refinement limits the space for carbide growth; therefore, the carbides' size has to decrease with the increasing withdrawal rate. For each casting, the mean volume fraction of carbides was calculated, with the value being in the range of 1.87 to 1.96 pct (Figure 11). The data obtained during these experiments indicate that an increase in withdrawal rate can lead to a slight decrease in carbide volume fraction. It should be mentioned that due to the variously shaped carbides and local differences in their concentration, a relatively large standard deviation was registered.

To provide a driving force for MC-type carbide growth, a sufficient degree of solute supersaturation is necessary. Enriching the interdendritic spaces in alloying elements provides sufficient solute for MC carbide growth and obtaining their relatively high volume fraction. To analyze in detail the differences in the main carbide former concentrations, additional SEM-EDX measurements were carried out *via* point analysis (Figure 12), and the semi-quantitative results are presented in Table V.

For each casting variant, 4 carbides (points) were selected within a given area for chemical composition analyzes to determine the concentration of strong carbide formers. The carbides in casting LP3W contain high concentrations of Hf and Ta, where point 1 contained 41.4 at pct and 23.9 at pct, respectively, as well as 11.4 at pct Ti and 6.2 at pct W. For points 2–4, the Hf contents decreased in favor of Ta and Ti. The Hf-rich carbide is closer to the $\gamma - \gamma'$ eutectic, indicating that it precipitated directly from the liquid phase in the earlier stages of solidification. In casting LP5W, all analyzed carbides were rich in Ta and Ti, *i.e.*, in the range of 36.8 to 38.4 at pct and 24.8 to 27.4 at pct, respectively. Points 5, 6, and 8 contained > 10 at pct Hf and < 10 at pct W, while for point 7, the opposite relationship was found. A similar trend was discovered in casting HP3W for points 9, 11, and 12 *vs* point 10. Point 13 of casting HP5W exhibited high Hf concentrations, similar to point 1 of casting LP3W; however, the Ti and W contents did not exceed 10 at pct. For

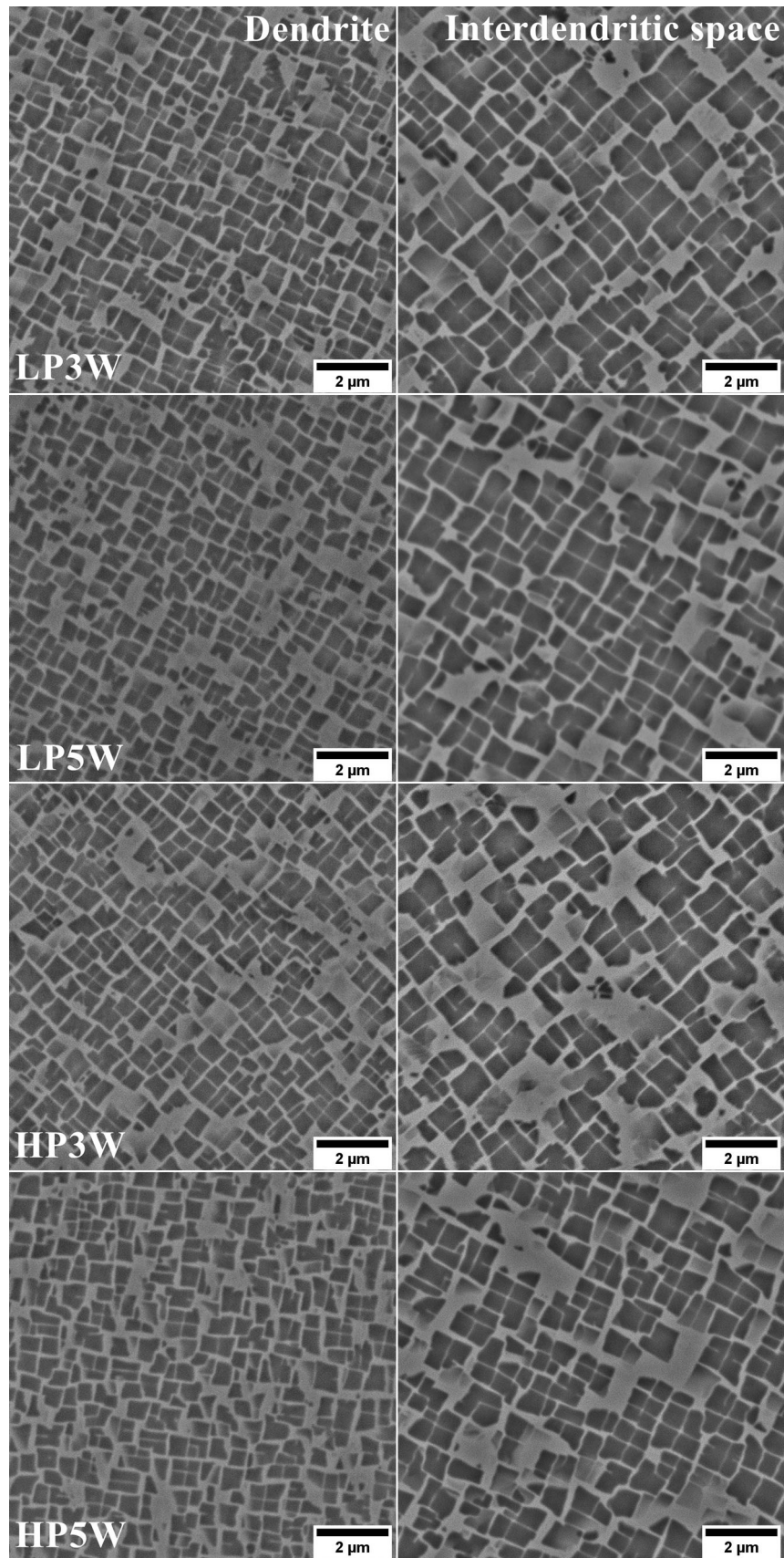


Fig. 6—Morphology of the secondary γ' precipitates in the dendritic regions and interdendritic spaces of the as-cast DS MAR-M247[®] castings, SEM-BSE.

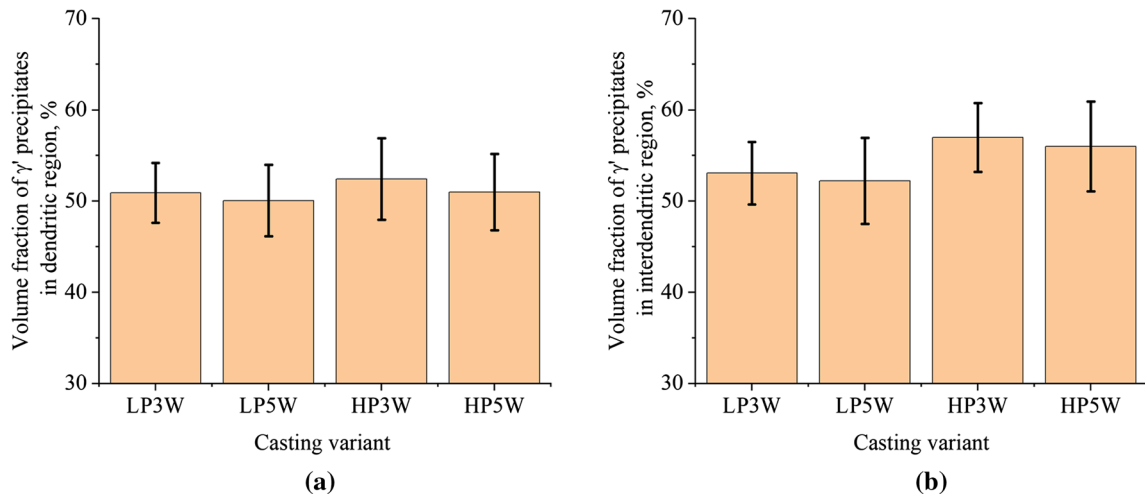


Fig. 7—Mean volume fraction of the γ precipitates: (a) in the dendritic regions; (b) in interdendritic spaces.

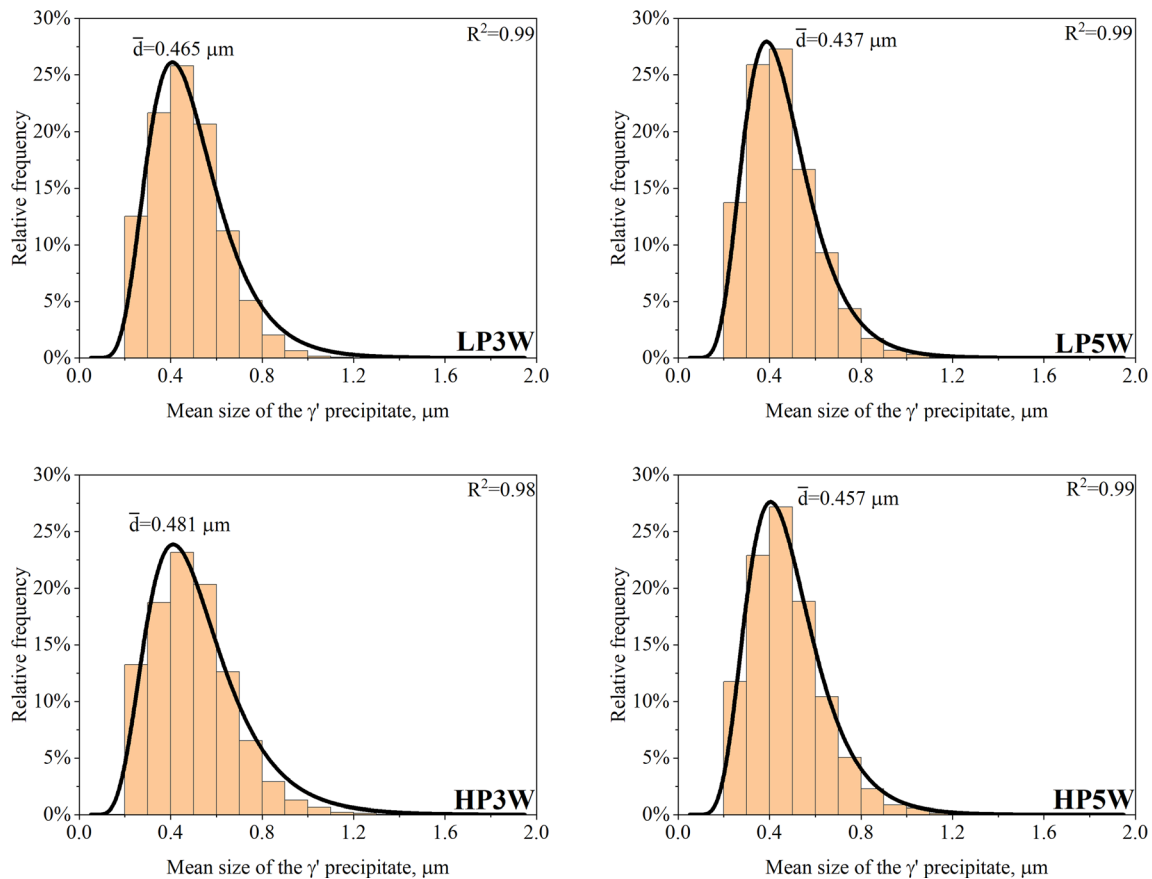


Fig. 8—Histogram of the mean secondary γ precipitates size in dendritic regions in as-cast DS MAR-M247[®] castings.

points 14 to 16, an increase in Ta and Ti and decrease in Hf was observed.

Carbide formation begins within an interdendritic liquid containing sufficient amounts of segregated alloying elements, like Ta, Hf, Ti, and Zr. Based on thermodynamical simulations, the phase transformation can proceed as $L \rightarrow \gamma + MC$, where M represents enriched Ta, Hf, and/or Ti in the liquid phase, providing

a sufficient chemical driving force for carbide precipitation. Transition elements with fewer electrons in their d-subshell have a stronger affinity to carbon atoms, and therefore, it is easier for them to create carbides. Ta, Hf, Ti, W, and Zr contain 3, 2, 2, 4, and 2 electrons in their d-subshell, respectively;^[24] therefore, the order of carbide formation would be HfC, TiC, TaC, ZrC, and WC. In the studied DS MAR-M247[®] superalloy, the

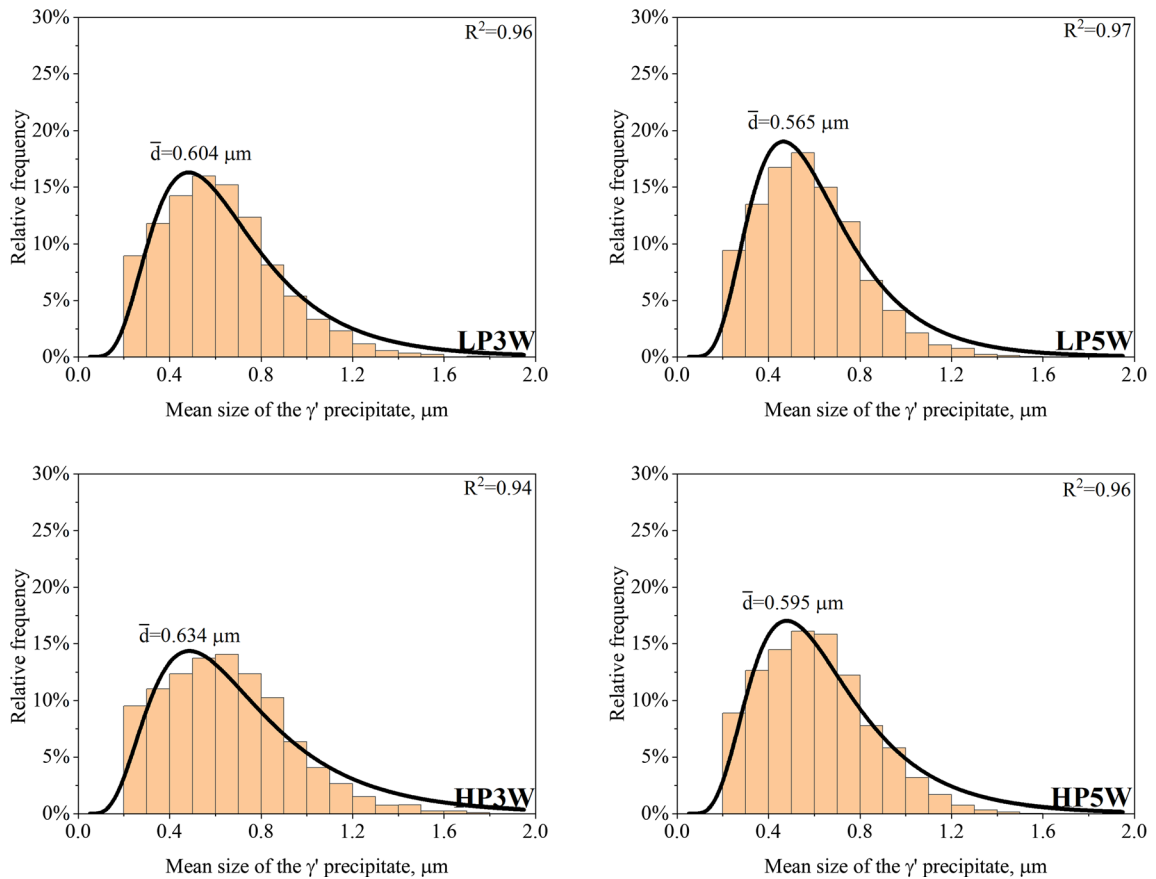


Fig. 9—Histogram of the secondary γ' precipitates in the interdendritic spaces in as-cast DS MAR-M247® castings.

strongest carbide former is Hf, which is added to directionally solidified superalloy castings to prevent grain boundary cracking during manufacturing.^[3] The presence of Hf alters the carbide's chemistry and morphology by tying up carbon into more stable Hf-containing MC carbides that form earlier or at higher temperatures during the solidification stage. The mutual relationship between Ta and Hf in MC carbides has been shown to influence their stability. In heat-treated René 108, characterized by a similar chemical composition as DS MAR-M247®, the stability of MC carbides with a dominant concentration of Hf or Ta was presented.^[25,26] The presence of $M_{23}C_6$ nano-carbides on the edges of MC carbides with higher Ta concentrations has also been reported, confirming that the phase transformation reaction $MC + \gamma \rightarrow M_{23}C_6 + \gamma'$ occurs during aging. In contrast, $M_{23}C_6$ nano-carbides have not been observed on blocky-shaped carbides with high Hf concentrations.

Precipitates with a phase contrast different from that of typical MC carbides and the γ' phase are observed in the interdendritic spaces of each casting (Figure 13). These gray-contrasting precipitates are characterized by a blocky-shaped morphology and their size can locally

exceed 1 μm . To reveal the chemical composition of these precipitates, semi-quantitative measurements were carried out and are summarized in Table VI. The dominant element in the precipitates is Cr, followed by W and Mo. The enrichment of precipitates in these elements suggests the presence of boride phases, such as M_5B_3 predicted by Thermo-Calc® simulations and detected *via* XRD. When dendrites do not overlap, carbides precipitate along their edges. With increased carbide formation, Hf and Ta are mostly consumed from the liquid phase. In turn, Mo, Cr, and W become more dominant in the liquid and are later consumed during the formation of W/Mo/Cr-rich borides.

Next, SEM-EDX point analysis was performed for lamellar-shaped precipitates (Figure 14). Three measurements were carried out directly on the precipitates, while three other within their vicinity. The precipitates mainly contain Ni and Hf, with their concentration ratios (Ni/Hf) being 4.0, 4.2, and 4.9 for points 1, 2, and 3, respectively (Table VII). While taking into account, the precipitates' thickness and the possibility of including Ni counts from the matrix, the studied precipitates are most likely the $Ni_7(Hf, Zr)_2$ phase. For points 4 and 5, Cr and W were detected, with Cr being the dominant

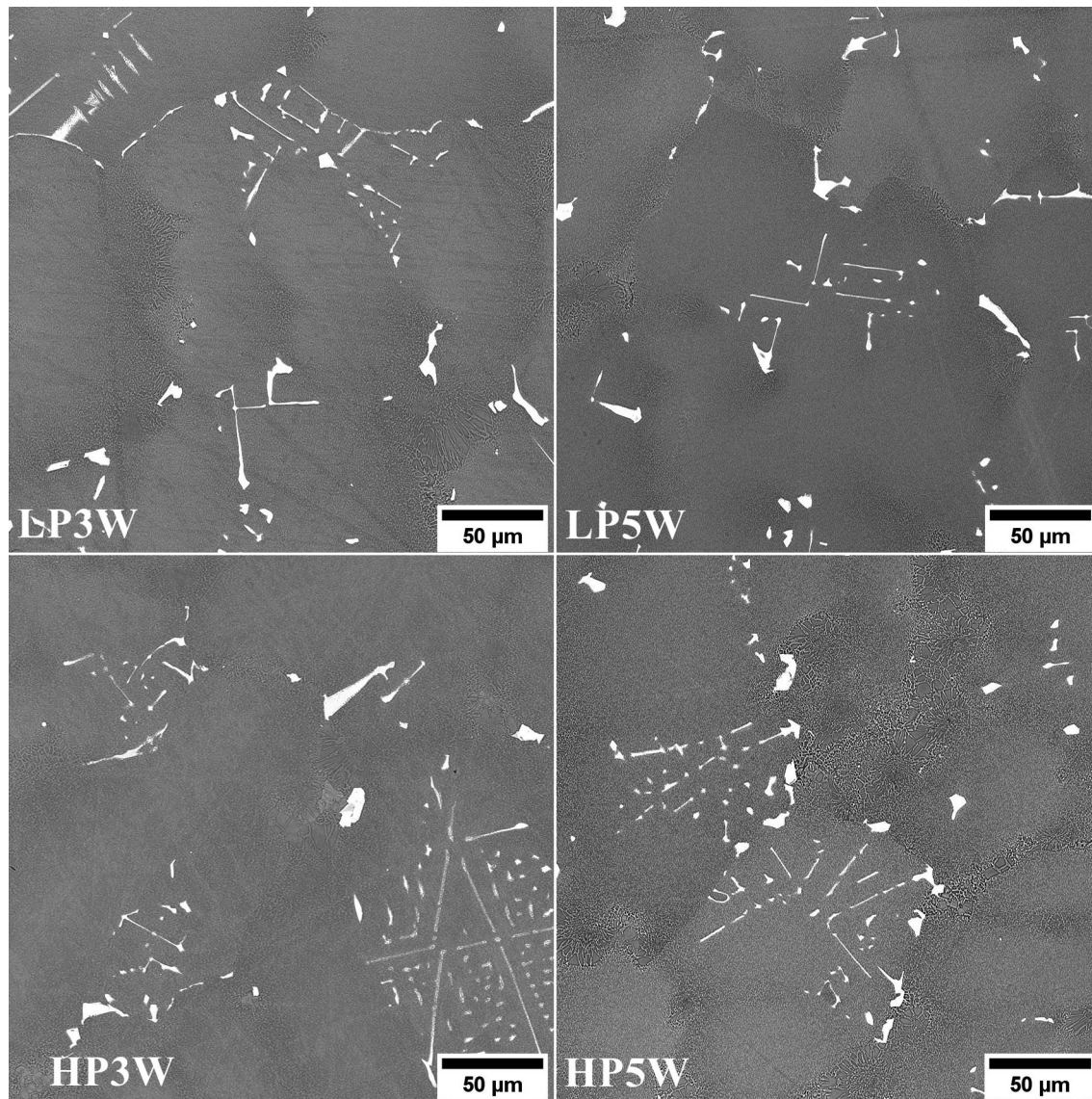


Fig. 10—Distribution and morphology of the MC carbides in as-cast DS MAR-M247[®] castings, SEM-BSE.

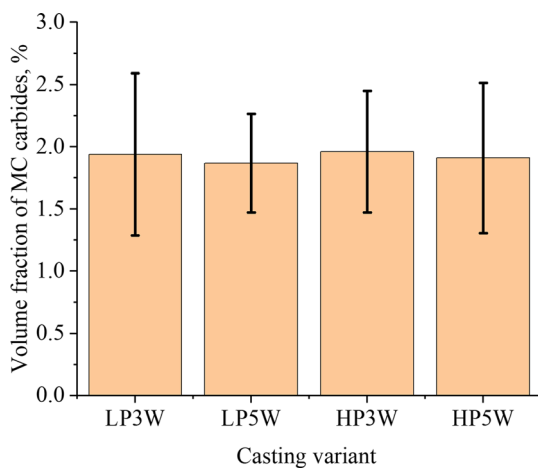


Fig. 11—MC carbides mean volume fraction.

element. Although it was suspected that these could be associated with the presence of borides, the contrast of these areas differ from that of borides, indicating at a different phase. For point 6, increased concentrations of Ni, Co, and Cr were registered, which most probably originate from the γ matrix.

Selected areas of the castings' interdendritic spaces were investigated using TEM. The first location includes the bulk bright (high Z -number) precipitate and the primary γ' precipitate, whereas the second was selected to investigate more morphologically complex precipitates. The presence of M_5B_3 boride [Figure 15(a–c)] and the $Ni_7(Hf, Zr)_2$ intermetallic phase [Figure 15(d, e)] precipitates in the vicinity of the primary γ' phase was confirmed. In the final stage of solidification, the eutectic reaction $L \rightarrow \gamma + \gamma'$ takes place in areas of Al- and Ti-enriched interdendritic liquid. As the solubility of Hf, Zr, and B in γ and γ' is extremely low, they segregate into the boundary ($\gamma - \gamma'$) eutectic-residual liquid

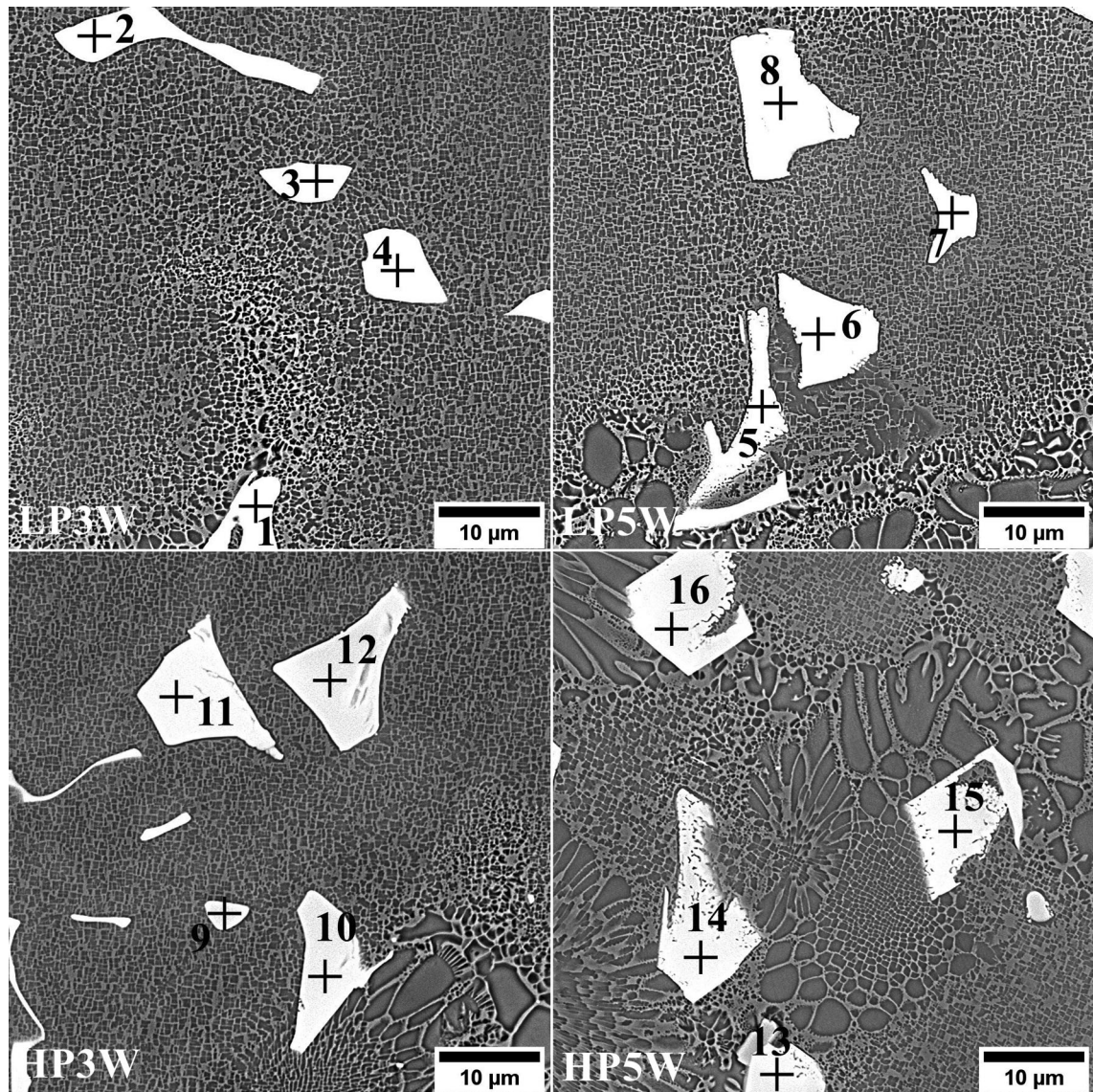


Fig. 12—Example SEM-EDX points in MC carbides in as-cast DS MAR-M247[®] castings, SEM-BSE.

interface and provide favorable precipitation conditions, *e.g.*, for Ni_7Zr_2 and M_5B_3 . $\text{Ni}_7(\text{Hf}, \text{Zr})_2$ intermetallic phase precipitates [Figure 16(a–c)] and M_3C_2 carbides [Figure 16(d, e)] in the second investigated region were also confirmed. The M_3C_2 carbides were not revealed during XRD due to their small size and low volume fraction. The carbides solidify in an orthorhombic crystal lattice with nominal lattice parameters of $a = 5.545 \text{ \AA}$, $b = 2.83 \text{ \AA}$, and $c = 11.47 \text{ \AA}$. Usually, the M position in these carbides is occupied by Cr. According to the binary Cr–C phase diagram, Cr_3C_2 carbides form through the peritectic reaction $\text{L} + \text{C} \rightarrow \text{Cr}_3\text{C}_2$. Additionally, the presence of $(\text{Cr}, \text{W})_3\text{C}_2$ carbides in the DS200 + Hf superalloy has been confirmed by Baldan.^[27] This type of carbide is not stable in heat-treated superalloys, and it is widely known that an

increase in the concentration of carbide-forming elements causes carbide formation to follow the sequence: $\text{M}_7\text{C}_3 \rightarrow \text{M}_{23}\text{C}_6 \rightarrow \text{M}_6\text{C} \rightarrow \text{MC}$.^[28]

According to the Ni–Hf binary diagram, the eutectic reaction $\text{L} \rightarrow \gamma + \text{Ni}_5\text{Hf}$ occurs at $1190 \text{ }^\circ\text{C}$.^[29] This stands in clear contrast with the presented results. Based on the equilibrium system, the Ni_7Hf_2 phase forms directly from the liquid at $1480 \text{ }^\circ\text{C}$. Next, two peritectic reactions take place: $\text{L} + \text{Ni}_7\text{Hf}_2 \rightarrow \text{Ni}_3\text{Hf}$ or $\text{L} + \text{Ni}_7\text{Hf}_2 \rightarrow \text{Ni}_5\text{Hf}$. The Ni_3Hf phase was found to form peritectically at $1350 \text{ }^\circ\text{C}$ from the liquid and Ni_7Hf_2 and to undergo a polymorphic transition ($\alpha \rightarrow \beta$) at $1200 \text{ }^\circ\text{C}$. It can be concluded that, at ambient temperature, no Ni_7Hf_2 occurs in the alloy's eutectics. To explain the presence of Ni_7Hf_2 in the eutectic, one should refer to the equilibrium systems of multi-element

Table V. Results of the Semi-quantitative SEM-EDX Analysis of MC Carbides in As-Cast DS MAR-M247® Castings, At Pet

Casting	Point	Ni	Co	Cr	Ta	W	Ti	Mo	Hf	Ta/Hf	(Ta + Hf)/(W + Ti)	(Ta/Hf)/(W + Ti)
LP3W	1	9.4	3.5	2.5	23.9	6.2	11.4	1.7	41.4	0.58	3.71	0.033
	2	7.1	1.5	1.4	39.6	7.8	27.2	2.1	13.3	2.99	1.51	0.085
	3	7.1	1.6	2.6	37.9	7.8	27.5	2.8	12.8	2.97	1.44	0.084
	4	8.0	1.8	2.1	38.5	8.2	27.6	2.2	11.6	3.31	1.40	0.093
LP5W	5	7.2	2.2	2.3	37.7	7.4	24.8	2.2	16.2	2.32	1.67	0.072
	6	7.7	2.2	2.3	38.3	8.8	27.4	2.3	11.0	3.48	1.36	0.096
	7	7.8	2.1	3.0	36.8	13.0	27.2	2.8	7.4	4.98	1.10	0.124
	8	5.9	2.2	1.9	38.4	7.3	26.1	2.4	15.8	2.43	1.62	0.073
HP3W	9	9.2	2.6	2.8	38.0	10.3	27.3	2.5	7.3	5.25	1.21	0.140
	10	5.4	1.0	1.4	40.5	7.7	29.1	2.4	12.6	3.23	1.45	0.088
	11	5.4	1.1	3.1	37.6	14.8	29.0	2.9	6.1	6.16	1.00	0.140
HP5W	12	8.2	4.5	5.5	31.9	12.0	24.9	5.0	8.1	3.95	1.08	0.107
	13	7.1	2.2	1.9	20.7	6.2	8.6	1.8	51.5	0.40	4.87	0.027
	14	4.4	0.8	1.3	40.1	6.0	25.7	2.5	19.2	2.09	1.87	0.066
	15	4.8	0.8	1.2	40.5	6.6	27.2	2.1	16.7	2.42	1.69	0.071
	16	5.2	1.5	1.3	40.3	7.2	27.2	2.3	15.1	2.68	1.61	0.078

alloys. It should be mentioned that the crystal structure of Ni_7Hf_2 was identified and found to be isotypic to Ni_7Zr_2 . Some of the Zr substitutes can indeed Hf in crystal lattice. Motejaded^[30] indicated that Zr-enriched residual liquid reacts with the eutectic phase or the primary γ' phase, according to reaction $\text{L} + \gamma' \rightarrow \gamma + \text{Ni}_7\text{Zr}_2$. The ternary eutectic reaction $\text{L} \rightarrow \gamma + \text{Ni}_7\text{Zr}_2 + \text{Ni}_5\text{Zr}$ is also possible. However, in DS MAR-M247® castings, the $\text{Ni}_5(\text{Hf}, \text{Zr})$ phase was not found. It should be taken into account that the presence of the Ni_5Hf phase cannot be completely excluded. As observed by Yunrong,^[31] Ni_5Hf near the $\gamma + \gamma'$ eutectic in Hf-containing Ni-based alloys can solidify with a dendritic structure. This illustrates the presence of a three-phase eutectic containing Ni_5Hf , with the possibility of γ and carbide adjacent to it. Babu^[32] showed that the formation of the $\gamma + \gamma'$ eutectic may be accompanied by the precipitation (from the residual liquid enriched in Zr and B) of a ternary eutectic, according to $\text{L} \rightarrow \gamma + \text{Ni}_7\text{Zr}_2 + \text{M}_3\text{B}_2$. In the vicinity of Ni_7Zr_2 in DS MAR-M247® castings, M_5B_3 borides and γ are detected. The Ni_7Hf_2 revealed in the TEM images possessed a block-like morphology and the lamellar. It can be stated that the formation of Ni_7Hf_2 in the interdendritic spaces of DS MAR-M247® castings can also be a part of the ternary eutectic with carbides or borides. According to Murata,^[33] the intermetallic phase $\text{Ni}_7(\text{Hf}, \text{Zr})_2$ is not stable in the medium temperature range and can undergo a phase transformation: $\text{MC} (\text{Ti rich}) + (\text{Ni}, \text{Co})_7(\text{Hf}, \text{Zr})_2 + \text{Cr} (\text{in matrix}) \rightarrow (\text{Hf}, \text{Zr})\text{C} + \text{Cr}_{23}\text{C}_6 + \gamma'$. The results suggest that liberated carbon atoms, formed through the decomposition of Ti-rich carbides, form Hf-rich and M_{23}C_6 carbides. It is well known that MC carbides transform into Cr_{23}C_6 carbides at intermediate temperatures (Cr originating from the matrix). The hafnium atoms, which form new Hf-rich carbides during thermal treatment, seem to originate from the $\text{Ni}_7(\text{Hf}, \text{Zr})_2$ compound. Considering the M_3C_2 carbides detected *via* TEM-SAED, it cannot be excluded that the Cr in the above-mentioned phase

transformation only originates from the matrix, as it may also come from the M_3C_2 phase.

F. DS MAR-M247® Castings Mechanical Properties of Characterization

The mechanical properties of the DS MAR-M247® castings were determined *via* tensile tests at room temperature. From the curves presented in Figure 17, it can be seen that castings HP3W and HP5W fabricated in molds preheated to 1566 °C (> than the pouring temperature 1538 °C) are characterized by higher strength and elongation in relation to the castings produced in molds preheated to 1510 °C. The casts from the higher temperature molds exhibited ultimate tensile strength (UTS) exceeding 1000 MPa, where for $v_s = 3.4$ mm/min, it was 1047 MPa and increased to 1088 MPa for $v_s = 5.0$ mm/min. The UTS values of the casts from lower temperature molds were 970 MPa and 989 MPa for withdrawal rates 3.4 and 5.0 mm/min, respectively. Castings HP3W and HP5W reach lower yield point values than castings LP3W and LP5W; however, they are characterized by higher elongation directly before rupture.

Based on the EMS-55447 specification,^[34] the minimum required yield and ultimate tensile strength for the DS MAR-M247® castings are 725 and 966 MPa, respectively. The presented results show that the selected parameters allowed obtaining castings that meet those requirements. Costa^[35] in the as-cast DS MAR-M247® produced with a withdrawal rate of 18 cm/h and fixed thermal gradient of 80 °C/cm obtained in compression test a yield strength (YS) at room temperature and at 600 °C equal to 796 and 671 MPa, respectively. Bor^[36] investigated the mechanical properties of DS MAR-M247® (withdrawal rate of 180 mm/h) in fully heat-treated condition. The ultimate tensile strength (UTS) of the produced castings was around 1000 MPa, whereas at 982 °C dropped to approximately 650 to 750 MPa. The high volume fraction of the γ' precipitates

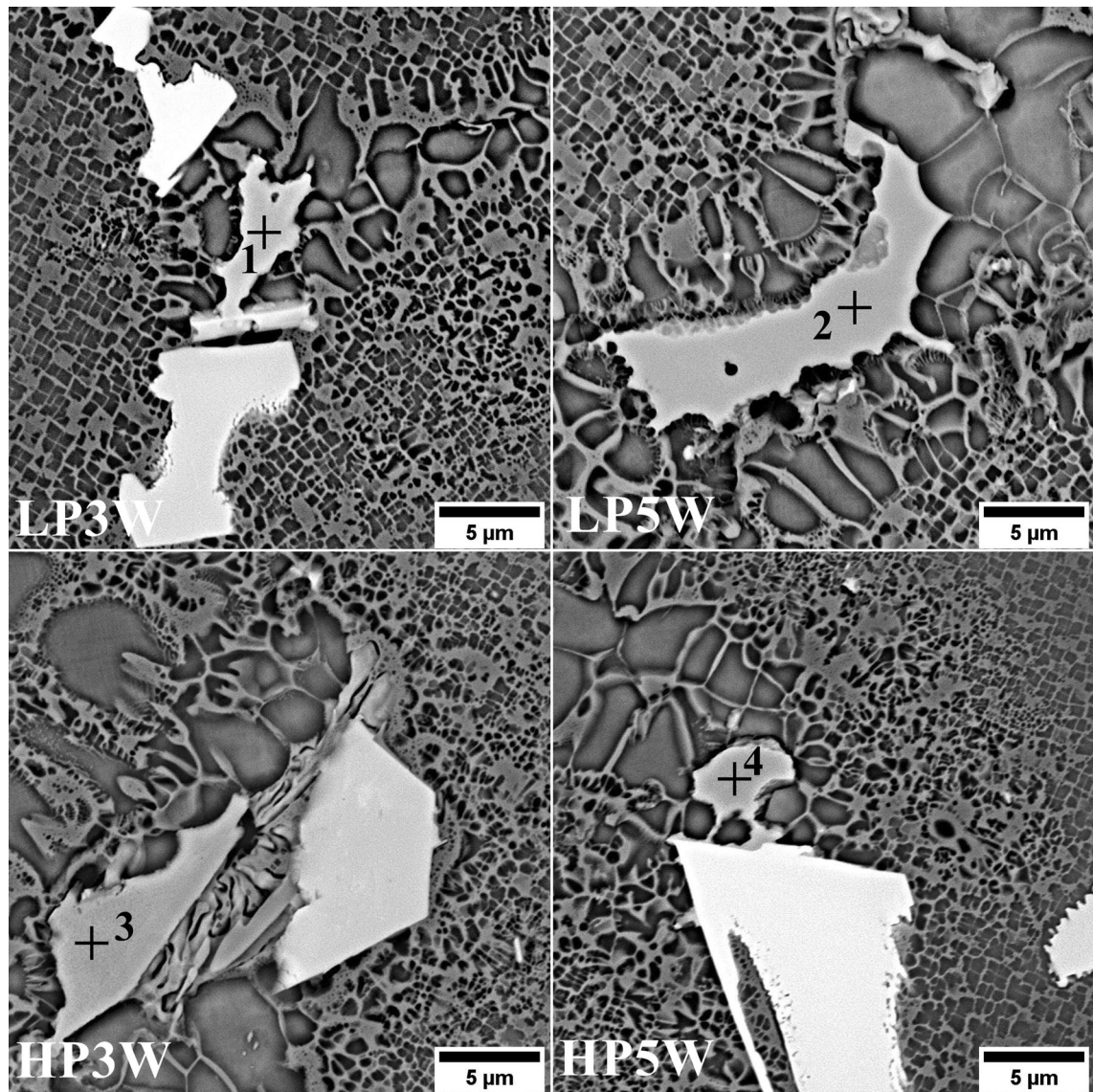


Fig. 13—Selected areas for semi-quantitative analysis of M_5B_3 precipitates in DS MAR-M247[®] castings.

Table VI. SEM-EDX Semi-quantitative Results of Points 1 to 4, at pct

Casting	Point	Ni	Co	Cr	Al	W	Mo
LP3W	1	14.8	4.2	45.6	5.7	20.8	9.1
LP5W	2	9.0	4.9	56.5	4.0	16.9	8.7
HP3W	3	12.5	3.7	44.1	6.2	24.5	8.9
HP5W	4	8.5	3.0	50.0	5.3	23.9	9.4

ensures the Ni-based superalloys desirable mechanical properties. An additional increase in strength results from the solution strengthening of the matrix and the presence of carbides and borides.^[6] In the γ matrix channels, the deformation occurs by dislocation slip in $\{111\} \langle 110 \rangle$ systems and at high temperatures by

transverse dislocation slip and climbing. As the temperature increases, the matrix strength decreases. The deformation of the γ' precipitates is realized as a result of dislocation slip also in the $\{111\} \langle 110 \rangle$ systems, and the total dislocation has a Burgers' vector of length $(a\sqrt{2})$, which is twice as long as in the γ phase. Complete dislocation slip from the matrix through the γ' phase is impossible without creating a high-energy defect called antiphase boundary (APB). Twice the length of the total dislocation vector in the γ' phase is associated with its four times higher energy. Reducing this energy requires the creation of superpartial dislocations, of which Burgers vector is shorter. The $a/2 \langle 101 \rangle$ dislocations must then move in pairs through the γ' intermetallic phase. Such a pair of partial dislocations, called a superdislocation, is connected by an antiphase boundary. They tend to change from $\{111\}$ to $\{100\}$ by

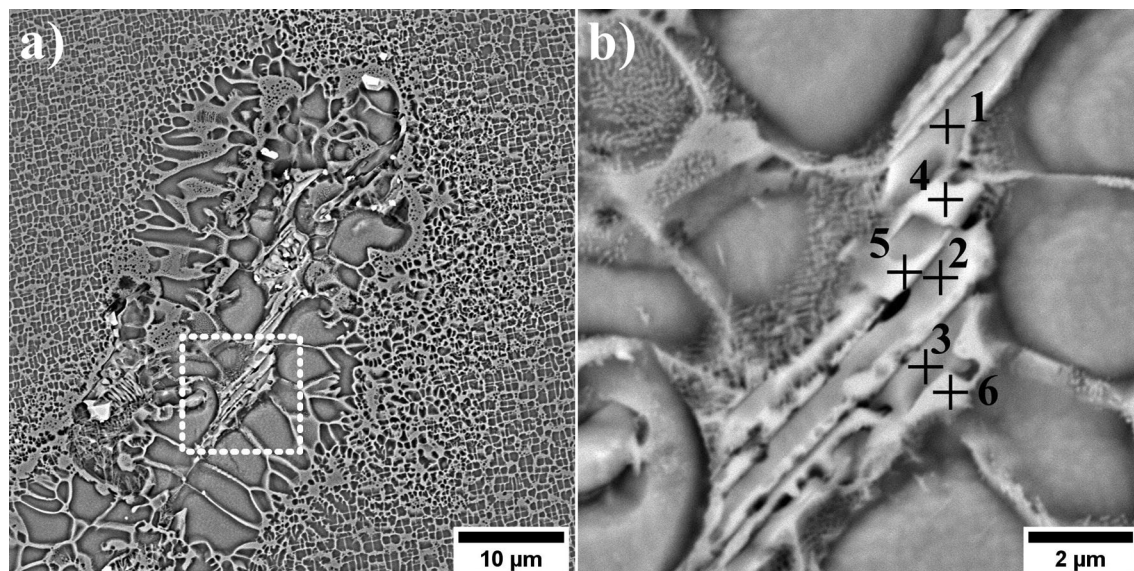


Fig. 14—(a, b) Selected points of SEM-EDX analysis in plate-like precipitates near the $\gamma - \gamma'$ eutectic, SEM-BSE.

Table VII. Semi-quantitative SEM-EDX Analysis Results from Plate-Like Precipitates Near the $\gamma - \gamma'$ Eutectic, At Pct

Element Point	Ni	Co	Cr	Ta	W	Ti	Mo	Hf	Zr	Al
1	59.1	8.2	10.3	1.8	—	0.8	0.7	14.6	1.7	—
2	61.2	9.8	6.3	2.0	—	0.7	0.4	14.5	1.9	—
3	61.5	10.7	7.8	2.0	—	0.6	0.4	12.6	1.4	—
4	17.3	5.7	50.0	0.9	8.8	0.4	7.2	2.6	1.9	5.4
5	24.3	6.1	42.7	0.9	6.1	0.3	6.1	4.2	2.4	6.7
6	48.7	14.9	18.3	1.5	0.3	0.6	1.3	2.2	0.8	11.3

transverse slip.^[37–39] The formation of dislocation anchor points accompanies this change, which increases with increasing temperature, leading to an increase in the strength of the γ' phase, which was first observed by Westbrook.^[40] Beardmore^[41] confirmed this phenomenon based on mechanical tests at elevated temperatures of a series of alloys from the Ni-Cr-Al triple system with different proportions of the γ' intermetallic phase. At the temperature of 700 to 900 °C, alloys containing at least 40 pct of γ' precipitates showed an increase in the yield point. With an amount of 80 pct of the γ' precipitates, the yield strength of the alloy was almost twice as high as at room temperature. The explanation of this phenomenon is directly related to the deformation mechanism of the ordered γ' phase. This work showed that as-cast DS MAR-M247[®] superalloy is characterized by the γ' precipitates having a volume fraction > 50 pct independently of the directional casting parameters. This allows us to conclude that the mechanical properties of the heat-treated DS MAR-M247[®] superalloy can be significantly enhanced during high-temperature service. After tensile testing,

the samples were subjected to fracture surface analysis *via* SEM. Selected fracture images are presented in Figure 18. All DS MAR-M247[®] castings exhibited a complex cracking nature. Brittle fracturing was observed for MC carbides and $\gamma - \gamma'$ eutectics. Large carbide precipitates, due to their high hardness and brittleness, contain numerous secondary cracks. The edges of those cracks are pronounced, with no indication of plastic deformation. In contrast, significant plastic deformation was observed for the γ matrix channels.

The microstructures of the fracture cross sections are shown in Figure 19. Numerous MC carbide precipitates and $\gamma - \gamma'$ eutectics are revealed on the edges, indicating crack propagation through interdendritic spaces. Furthermore, secondary γ' precipitate deformation is locally visible. Oxides or other non-metallic inclusions are not disclosed at the fracture edges. Further away from the main fracture, secondary cracks and fine pores occur locally, additionally occurring near carbides. Grain boundaries aligned parallel to the major stress axes facilitate crack initiation.

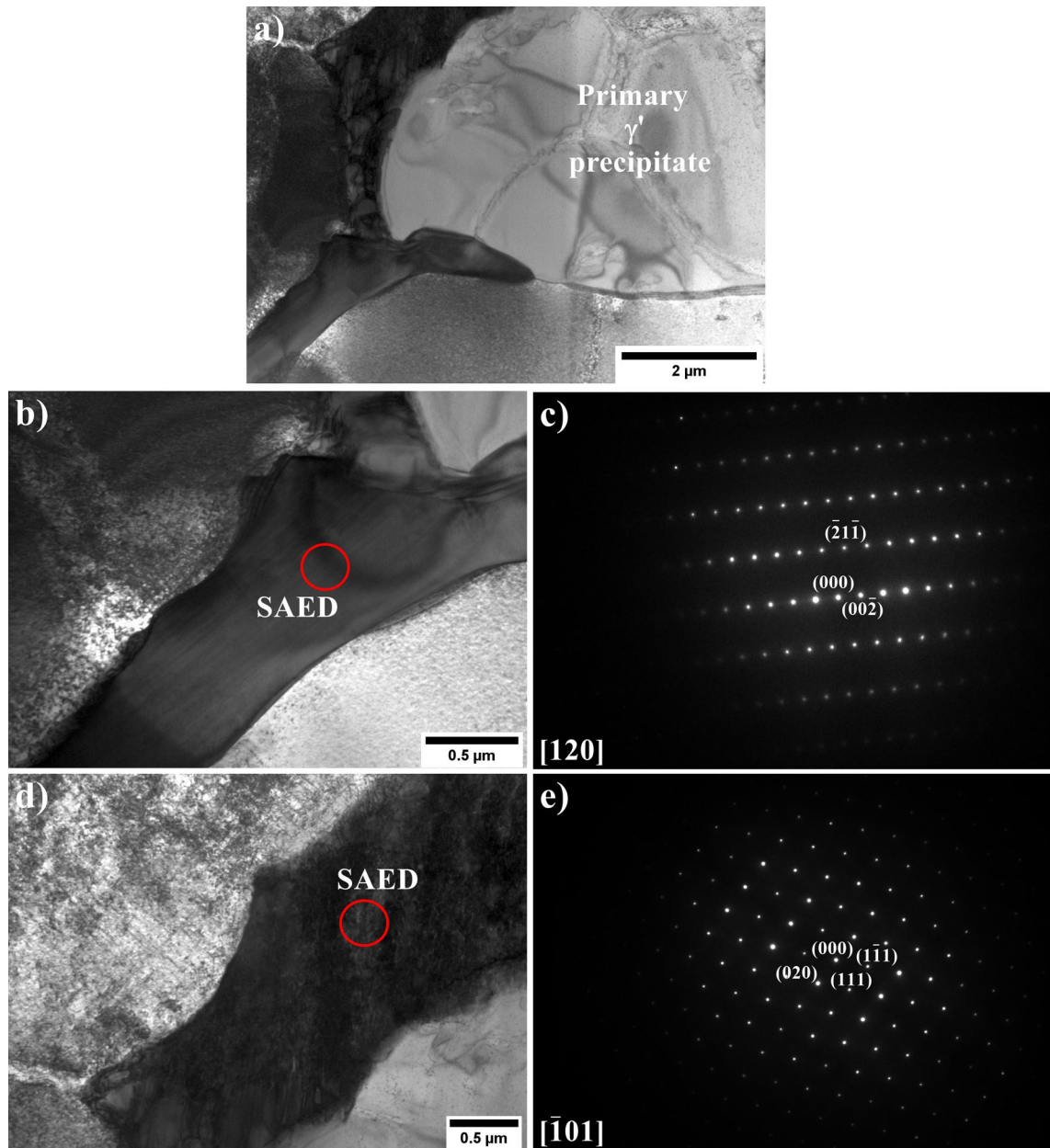


Fig. 15—(a) Investigated precipitate area, (b, c) morphology and SAED pattern of M_5B_3 and (d, e) $Ni_7(Hf, Zr)_2$.

IV. CONCLUSIONS

This work focused on characterizing the as-cast microstructure and resulting properties of directionally solidified MAR-M247[®], produced using different withdrawal rates and shell mold temperatures. The obtained results allowed to draw the following conclusions:

1. Primary and secondary dendrite arm spacings decrease with increasing withdrawal rate for both mold preheating temperatures. For the mold preheating temperature of 1510 °C and withdrawal rate of 3.4 mm/min, the PDAS and SDAS were 325 μm ($\pm 31 \mu\text{m}$) and 64 μm ($\pm 8 \mu\text{m}$), respectively. For the withdrawal rate of 5.0 mm/min, the values decreased to 303 μm ($\pm 34 \mu\text{m}$) and 56 μm ($\pm 6 \mu\text{m}$).
2. The largest \bar{d} for secondary γ' precipitates in dendritic regions was obtained in casting HP3W ($T_0 = 1566 \text{ }^\circ\text{C}$, $v_s = 3.4 \text{ mm/min}$) and was equal to 0.481 μm , which decreased to 0.457 μm for the longer withdrawal rate of 5.0 mm/min (casting HP5W). The same trend was observed between castings LP3W and LP5W. The same size vs technological parameter behavior was observed for secondary γ' precipitates in interdendritic

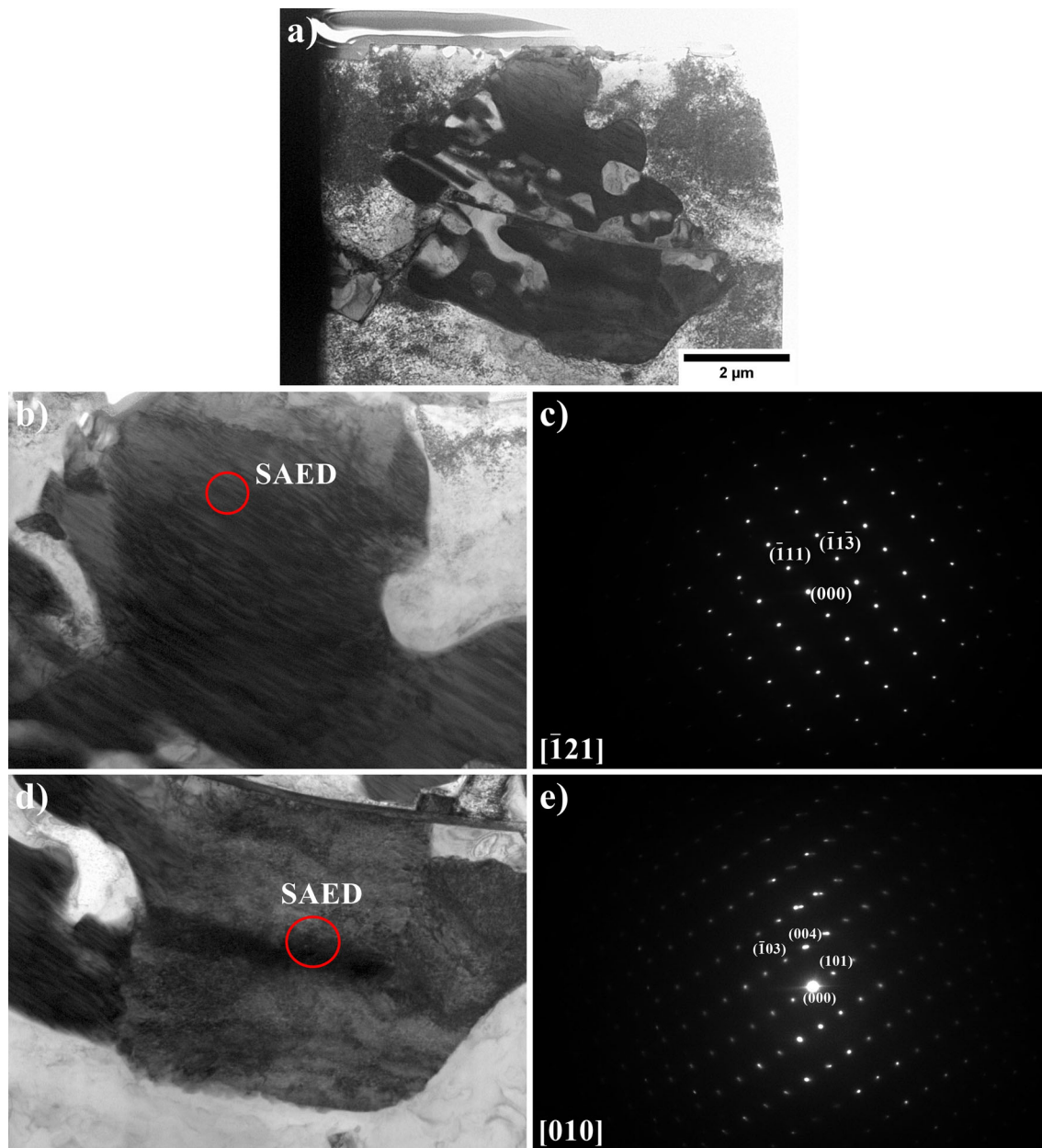


Fig. 16—(a) Investigated precipitate area, (b, c) morphology and SAED pattern of $\text{Ni}_7(\text{Hf}, \text{Zr})_2$ and (d, e) M_3C_2 .

spaces, despite their overall size being larger than those found in dendritic regions (*e.g.*, casting HP3W, $0.634 \mu\text{m}$ compared to $0.481 \mu\text{m}$).

3. The MC carbide volume fraction decreased with increasing withdrawal rate, *i.e.*, from 1.93 to 1.87 pct for $T_0 = 1510 \text{ }^\circ\text{C}$ and from 1.96 to 1.91 pct for $T_0 = 1566 \text{ }^\circ\text{C}$.

4. Besides γ' precipitates and MC carbides, M_5B_3 , $\text{Ni}_7(\text{Hf}, \text{Zr})_2$, and M_3C_2 phases were detected within the interdendritic spaces of the studied castings.

5. The castings produced in molds preheated to $1510 \text{ }^\circ\text{C}$ were characterized by lower UTS and elongation than castings produced in molds preheated to $1566 \text{ }^\circ\text{C}$, with the highest UTS value of

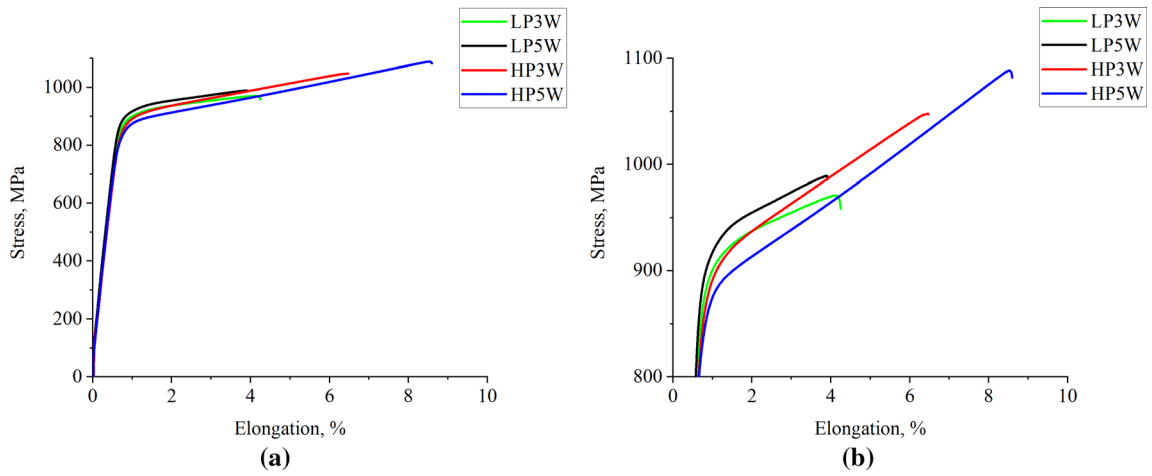


Fig. 17—Tensile test curves of the as-cast DS MAR-M247[®] castings: (a) 0 to 1100 MPa range; (b) 800 to 1100 MPa range.

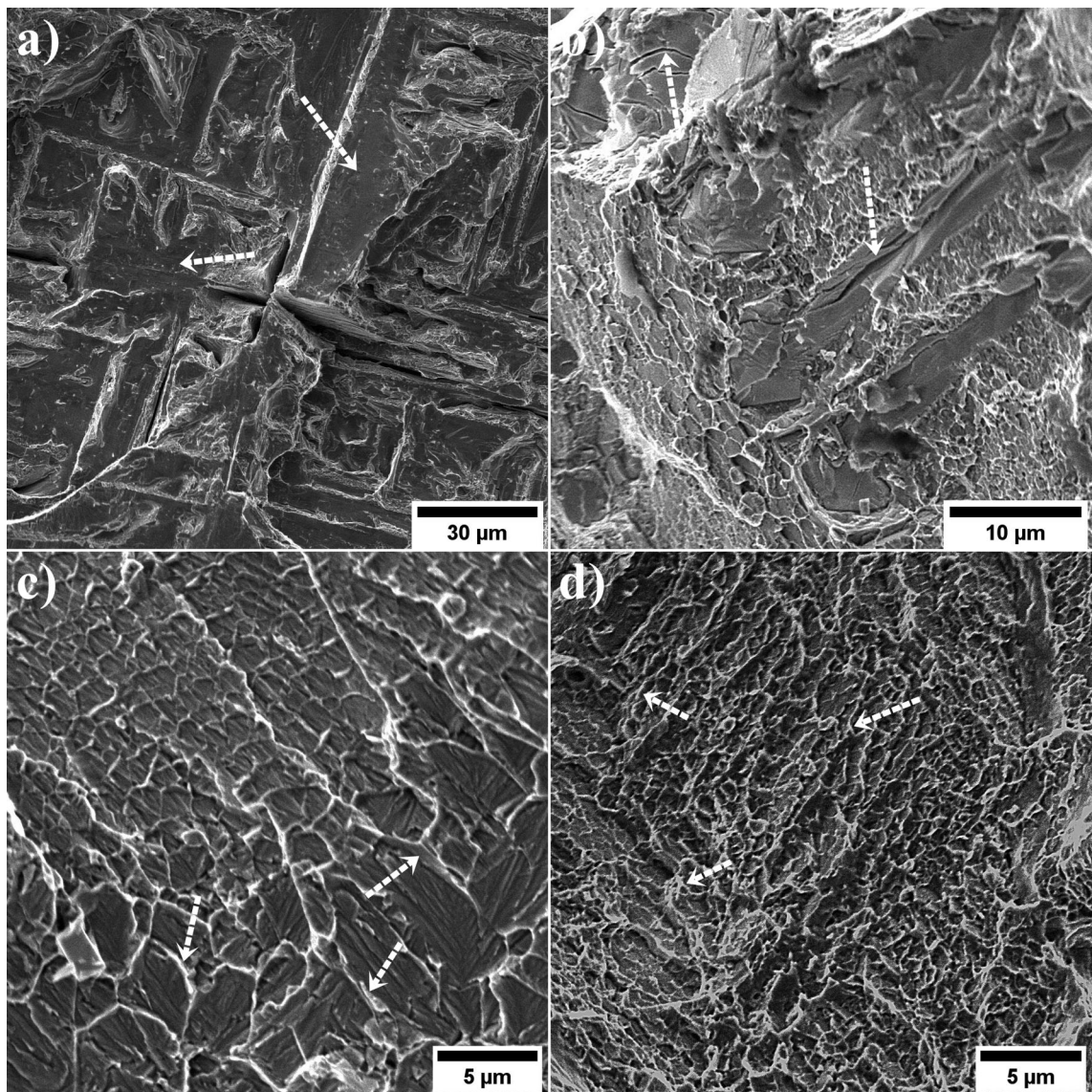


Fig. 18—Selected higher magnification fracture images: (a) brittle fracture of carbides; (b) secondary fracture of carbides; (c) plastic deformation of the matrix in the area of the eutectic $\gamma - \gamma'$; (d) plastic deformation of the matrix in the dendritic region, SEM-SE.

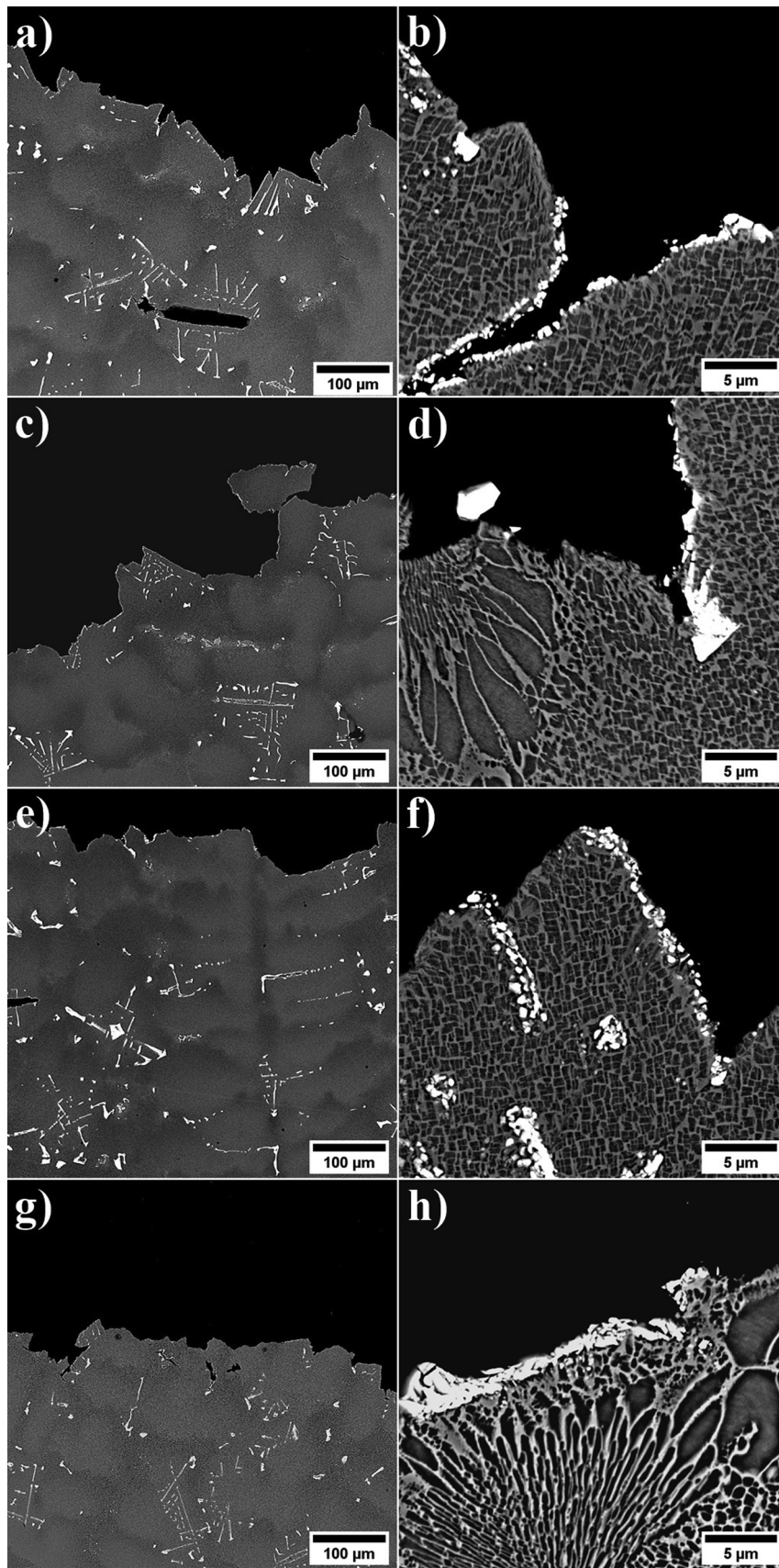


Fig. 19—Cross-sectional fracture morphologies of DS MAR-M247[®] castings: (a, b) LP3W; (c, d) LP5W; (e, f) HP3W; (g, h) HP5W, SEM-BSE.

1088 MPa registered for a withdrawal rate of 5.0 mm/min.

ACKNOWLEDGMENTS

The authors gratefully acknowledge the funding by National Centre for Research and Development, Poland, under Grant POIR.01.01.01-00-1335/20. ŁR has been partly supported by the Foundation for Polish Science (FNP) with scholarship START 2022 (no. START 066.2022). ŁR and TK also thank to the Polish Ministry of Science and Higher Education, statutory number 16.16.110.663.

CONFLICT OF INTEREST

The authors declare that they have no known competing financial interests or personal relationships that could have appeared to influence the work reported in this paper.

ETHICAL APPROVAL

This article does not contain any studies with human participants or animals performed by any of the authors.

OPEN ACCESS

This article is licensed under a Creative Commons Attribution 4.0 International License, which permits use, sharing, adaptation, distribution and reproduction in any medium or format, as long as you give appropriate credit to the original author(s) and the source, provide a link to the Creative Commons licence, and indicate if changes were made. The images or other third party material in this article are included in the article's Creative Commons licence, unless indicated otherwise in a credit line to the material. If material is not included in the article's Creative Commons licence and your intended use is not permitted by statutory regulation or exceeds the permitted use, you will need to obtain permission directly from the copyright holder. To view a copy of this licence, visit <http://creativecommons.org/licenses/by/4.0/>.

REFERENCES

1. R. Reed: *The Superalloys: Fundamentals and Applications*, Cambridge University Press, Cambridge, 2006.
2. W. Xuan, C. Li, D. Zhao, B. Wang, C. Li, Z. Ren, Y. Zhong, X. Li, and G. Cao: *Metall. Mater. Trans. B*, 2017, vol. 48, pp. 394–405. <https://doi.org/10.1007/s11663-016-0823-6>.
3. C. Sims, S. Stoloff, and W. Hagel: *Superalloys II*, Wiley-Interscience, New York, 1987.
4. D. Szeliga: *Metall. Mater. Trans. A*, 2022, vol. 53, pp. 3224–31. <https://doi.org/10.1007/s11661-022-06752-9>.

5. X. Wang, T. Huang, W. Yang, Q. Yue, C. He, P. Qu, J. Zhang, and L. Liu: *Vacuum*, 2021, vol. 183, p. 109800. <https://doi.org/10.1016/j.vacuum.2020.109800>.
6. Ł Rakoczy, M. Grudzień, and R. Cygan: *J. Mater. Eng. Perform.*, 2019, vol. 28, pp. 3826–34. <https://doi.org/10.1007/s11665-018-3853-1>.
7. P. Peng, L. Lu, Z. Liu, Y. Xu, X. Zhang, Z. Ma, H. Zhang, M. Guo, and L. Liu: *J. Alloys Compd.*, 2022, vol. 927, p. 167009. <https://doi.org/10.1016/j.jallcom.2022.167009>.
8. J. Nawrocki, M. Motyka, D. Szeliga, W. Ziaja, R. Cygan, and J. Sieniawski: *J. Manuf. Process.*, 2020, vol. 49, pp. 153–61. <https://doi.org/10.1016/j.jmapro.2019.11.028>.
9. J. Xiao, W. Jian, D. Han, K. Li, Y. Lu, and L. Lou: *J. Alloys Compd.*, 2022, vol. 898, p. 162782. <https://doi.org/10.1016/j.jallcom.2021.162782>.
10. S. Gu, H. Gao, Z. Wen, H. Pei, Z. Li, Y. Zhao, and Z. Yue: *J. Alloys Compd.*, 2021, vol. 884, p. 161055. <https://doi.org/10.1016/j.jallcom.2021.161055>.
11. Q. Li, H. Zhang, Y. Cheng, M. Du, M. Gao, T. Hong, Y. Lin, and H. Zhang: *J. Alloys Compd.*, 2022, vol. 923, p. 166930. <https://doi.org/10.1016/j.jallcom.2022.166930>.
12. K. Liu, J. Wang, Y. Yang, and Y. Zhou: *J. Alloys Compd.*, 2021, vol. 883, p. 160723. <https://doi.org/10.1016/j.jallcom.2021.160723>.
13. Y. Zhao, M. Zhang, L. Yang, Y. Guo, J. Zhang, H. Lu, Y. Chen, and D. Tang: *Progress Nat. Sci.: Mater. Int.*, 2021, vol. 31, pp. 493–500. <https://doi.org/10.1016/j.pnsc.2021.04.010>.
14. E. Scheil: *Z. Metallkd.*, 1942, vol. 34, pp. 70–72.
15. N. Saunders: in *Proceedings of the Superalloys 1996*, Warrendale, Pennsylvania, 1996.
16. C. Walter, B. Hallstedt, and N. Warnken: *Mater. Sci. Eng. A*, 2005, vol. 397(1–2), pp. 385–90. <https://doi.org/10.1016/j.msea.2005.02.056>.
17. Ł Rakoczy, M. Grudzień-Rakoczy, B. Rutkowski, R. Cygan, F. Hanning, G. Cios, S. Habisch, J. Andersson, P. Mayr, and A. Zielińska-Lipiec: *Arch. Civ. Mech. Eng.*, 2023, vol. 23, p. 119. <https://doi.org/10.1007/s43452-023-00659-x>.
18. A. Mirak and M. Fathi: *Mater. Charact.*, 2022, vol. 104, p. 112449. <https://doi.org/10.1016/j.matchar.2022.112449>.
19. T. Grosdidier, A. Hazotte, and A. Simon: *Mater. Sci. Eng. A*, 1998, vol. 256, pp. 183–96. [https://doi.org/10.1016/S0921-5093\(98\)00795-3](https://doi.org/10.1016/S0921-5093(98)00795-3).
20. M. Doi, T. Miyazaki, and T. Wakatsuki: *Mater. Sci. Eng.*, 1984, vol. 67, pp. 247–53. [https://doi.org/10.1016/0025-5416\(84\)90056-9](https://doi.org/10.1016/0025-5416(84)90056-9).
21. A. Ardell: *Interface Sci.*, 1995, vol. 3, pp. 119–25. <https://doi.org/10.1007/BF00207013>.
22. A. Bhambri, T. Kattamis, and J. Morral: *Metall. Trans. B*, 1975, vol. 6, pp. 523–37. <https://doi.org/10.1007/BF02913844>.
23. N. D'Souza, H. Dong, M. Ardakani, and B. Shollock: *Scripta Mater.*, 2005, vol. 53, pp. 729–33. <https://doi.org/10.1016/j.scriptamat.2005.05.012>.
24. D. Kim, G. Lee, D. Kim, and S. Jeong: *J. Mater. Sci. Technol.*, 2013, vol. 29, pp. 1184–90. <https://doi.org/10.1016/j.jmst.2013.09.022>.
25. Ł Rakoczy, B. Rutkowski, M. Grudzień-Rakoczy, R. Cygan, W. Ratuszek, and A. Zielińska-Lipiec: *Materials*, 2020, vol. 13, p. 4452. <https://doi.org/10.3390/ma13194452>.
26. Ł Rakoczy, M. Grudzień-Rakoczy, F. Hanning, G. Cempura, R. Cygan, J. Andersson, and A. Zielińska-Lipiec: *Metall. Mater. Trans. A*, 2021, vol. 52, pp. 4767–84. <https://doi.org/10.1007/s11661-021-06420-4>.
27. A. Baldan: *J. Mater. Sci.*, 1991, vol. 26, pp. 3879–90. <https://doi.org/10.1007/BF01184986>.
28. A. Jena and M. Chaturvedi: *J. Mater. Sci.*, 1984, vol. 19, pp. 3121–39. <https://doi.org/10.1007/BF00549796>.
29. P. Nash and A. Nash: *Bull. Alloy Phase Diagr.*, 1983, vol. 4, pp. 250–53. <https://doi.org/10.1007/BF02868664>.
30. H. Motejadded, M. Soltanieh, and S. Rastegari: *J. Mater. Sci. Technol.*, 2011, vol. 27(10), pp. 885–92. [https://doi.org/10.1016/S1005-0302\(11\)60160-6](https://doi.org/10.1016/S1005-0302(11)60160-6).
31. Z. Yunrong, W. Yuping, X. Jizhou, P. Caron, and T. Khan: in *Superalloys 1988*, Champion, Pennsylvania, 1988. https://doi.org/10.7449/1988/superalloys_1988_335_344.
32. S. Babu, S. David, J. Vitek, and M. Miller: *J. Phys. IV Proc.*, 1996, vol. 06(C5), pp. 253–58. <https://doi.org/10.1051/jp4:1996541>.

33. Y. Murata, R. Ninomiya, and N. Yukawa: *Scripta Metall.*, 1988, vol. 22, pp. 21–6. [https://doi.org/10.1016/S0036-9748\(88\)80299-0](https://doi.org/10.1016/S0036-9748(88)80299-0).
34. Allied-Signal Aerospace Company: Engine Materials Specification 55447. Castings, Investment, MAR-M247. Phoenix; Allied-Signal Aerospace Company: 1988.
35. A.M.S. Costa, E.S.N. Lopes, R.J. Contieri, R. Caram, R. Baldan, G.E. Fuchs, and C.A. Nunes: *J. Mater. Eng. Perform.*, 2019, vol. 28(4), pp. 2427–38. <https://doi.org/10.1007/s11665-019-04014-1>.
36. H.-Y. Bor, C.-N. Wei, A.-C. Yeh, W.-B. He, H.-S. Wang, and C.-M. Kuo: Heat treatment effects on the high temperature mechanical behavior of directionally solidified MAR- M247 superalloy, in *The 8th Pacific Rim International Congress on Advanced Materials and Processing*. F. Marquis, ed., TMS (The Minerals, Metals & Materials Society), 2013, pp. 379–86. https://doi.org/10.1007/978-3-319-48764-9_46.
37. J. Rame, D. Eyidi, A. Joulain, M. Gauthe, and J. Cormier: *Metall. Mater. Trans. A*, 2023, vol. 54, pp. 1496–508. <https://doi.org/10.1007/s11661-023-07022-y>.
38. S. Hamadi, F. Hamon, J. Delautre, J. Cormier, P. Villechaise, S. Utada, P. Kontis, and N. Bozzolo: *Metall. Mater. Trans. A*, 2018, vol. 49, pp. 4246–61. <https://doi.org/10.1007/s11661-018-4748-3>.
39. J.-B. le Graderend, J. Cormier, F. Gallerneau, P. Villechaise, S. Kruch, and J. Mendez: *Int. J. Plast.*, 2014, vol. 59, pp. 55–83. <https://doi.org/10.1016/j.ijplas.2014.03.004>.
40. J. Westbrook: *J. Min. Met. Mater. Soc.*, 1957, vol. 9, pp. 898–904. <https://doi.org/10.1007/BF03397938>.
41. P. Beardmore, R. Davies, and T. Johnston: *Trans. Metall. Soc. AIME*, 1969, vol. 245, pp. 1537–45.

Publisher's Note Springer Nature remains neutral with regard to jurisdictional claims in published maps and institutional affiliations.